DIAGNOSIS AND IMPROVEMENT OF CRYOSPHERE SHORTWAVE RADIATION BIASES IN GLOBAL CLIMATE MODELS

by

Justin Perket

A dissertation submitted in partial fulfillment
of the requirements for the degree of
Doctor of Philosophy
(Applied Physics)
in the University of Michigan
2015

Doctoral Committee:

Assistant Professor Mark Flanner, Chair
Assistant Professor Brian Arbic
Assistant Professor Jeremy N. Bassis
Associate Professor Xianglei Huang
Assistant Professor Gretchen Keppel-Aleks

Dedication

To my parents

Acknowledgements

I would like to thank my advisor, Mark Flanner, who has been a consistent source of helpful advice, encouragement, and cheerfulness in his mentorship. It's been an excellent experience being part of the research group since the beginning of his Michigan career. Thanks goes out to my committee for the helpful comments on my dissertation.

I would also like to thank my collaborators for their helpful support: Jen Kay, for our work in cryosphere and cloud forcings, and Martyn Clark and Dave Lawrence for our work in vegetation canopy interception. They have been exceptional to work with during my grad student career with their mentorship and knowledge of areas I knew little about at first. The NCAR scientists have been great to work with and learn from during my visit. I would like to acknowledge high-performance computing support from Yellowstone (ark:/85065/d7wd3xhc) provided by NCAR's Computational and Information Systems Laboratory, as well as from Flux provided by Advanced Research Computing at the University of Michigan.

Additionally, the faculty and in both Applied Physics and AOSS are excellent. I've taken great classes here at Michigan, learned a ton, and enjoyed the friendliness and camaraderie in both programs. Not only in grad school, but continuously through undergrad and high school, there were superb educators encouraging me to always learn more.

Last, and not at all least, I am exceptionally lucky to have befriended some amazing people while attending Michigan. It's the support of friends that has made enduring grad school possible. The many adventures, outings and conversations we've had is what made Ann Arbor a treasured home.

Table of Contents

List of Tables

List of Figures

List of Acronyms and Initialisms

CAM – Community Atmosphere Model
CCSM – Community Climate System Model
CESM – Community Earth System Model
CICE – Community Ice CodE
CLM – Community Land Model
CMIP – Coupled Model Intercomparison Project
CRF – Cloud radiative forcing
CrRE – Cryosphere radiative effect
ESM – Earth System Model
ET - Evapotranspiration
GCM – Global climate model, General circulation model
G-RMSE – Gridcell-averaged Root Mean Square Error
LAI – Leaf Area Index
MODIS – - MODerate Resolution Imaging Spectroradiometer
NH – North Hemisphere
NIR – Near Infrared
NVDSW – Net Visible Direct Shortwave
PFT – Plant Functional Type
PILPS – Project for the Intercomparison of Land-Surface Parameterization Schemes
POP – Parallel Ocean Program
ppm – parts per million
RCP – Representative Concentration Pathway
RF – Radiative Forcing
R-RMSE – Regionally averaged Root Mean Square Error
SAF – Snow Albedo Feedback
SAI – Stem Area Index
SH – South Hemisphere
SnowMIP – Snow Model Intercomparison Project
SWE – Snow water equivalent
TOA – Top of atmosphere
TOM – Top of model
VBSA – Visible Black-sky albedo
VDALN – Visible Direct Albedo at Local Noon

Abstract

Diagnosis and Improvement of Cryosphere Shortwave Radiation Biases in Global Climate Models

by

Justin Perket

Mark Flanner, Chair

Faithful representation of cryospheric change is critical for accurate climate modeling, but there are complicating issues in representing snow extent and reflectance in physically realistic ways. This thesis is a collection of diagnostics and improvements of cryospheric shortwave radiation in climate models. Firstly, we incorporate a diagnostic called the cryosphere radiative effect (CrRE), the instantaneous influence of surface snow and sea ice on the top-of-model solar energy budget, into two released versions of the Community Earth System Model. CrRE offers a more climatically relevant metric of the cryospheric state than snow and sea ice extent and is influenced by factors such as the seasonal cycle of insolation, cloud masking, and vegetation cover. We evaluate CrRE during the late 20th century and over the 21st century, specifically diagnosing the CrRE contributions from terrestrial and marine sources. Present-day boreal CrRE compares well with observationally derived estimates. Similar present-day CrRE in the two model versions results from compensating differences in cloud masking and sea ice extent.

Radiative forcing in future warming scenarios reduces boreal and austral sea ice cover, and boreal snow cover, which each contribute roughly 1 W/m^2 to enhancing global absorbed shortwave radiation. Similar global cryospheric albedo feedbacks between 0.41-0.45 $W/m^2/K$ indicate the models exhibit similar temperature-normalized CrRE change.

Secondly, we incorporated a modified canopy scheme into the Community Land Model with snow interception as a prognostic variable and snow unloading tuned to in-situ measurements. The canopy radiation scheme has been updated from a direct temperature dependence of optical parameters to a dependence on the prognostic snow storage. With these improvements, boreal forest zones show large, significant albedo error reductions relative to MODIS observations. 13% gridcell RMSE reduction during spring results from a more gradual seasonal transition in albedo, while 27% reduction in winter is from a lower albedo. Over all North Hemisphere land area, error was also reduced. Thirdly, we assess the impacts of the snow canopy vegetation treatment in coupled model warming scenarios. Little change in global albedo feedback or climate sensitivity were shown, but significant alterations resulted that varied both regionally and temporally.

Chapter 1

Introduction

1.1 What is a Global Climate Model?

A Global Climate Model (GCM) is a three-dimensional numerical simulation to predict climate. At minimum, all GCMs must contain a General Circulation Model (also GCM, the terms are somewhat conflated) that is capable of calculating the transfer of energy, mass and momentum on the sphere of the Earth. Three-dimensional atmosphere models are most directly related to climate predictions, but ocean circulation models are also required to accurately predict the flow of heat and moisture around the globe. Land surface models provide important lower boundary conditions to the atmosphere. They represent surfaces composed of soil, vegetation, and different forms of water: lakes, rivers, snowpack, and glaciers. Land models sometime include sub-models to handle the complexities of glaciers, rivers, or other components. The land model simulates both reception and reemission of energy and moisture from the atmosphere.

Current-generation GCM's typically have a horizontal resolution of 1-2 degrees across the Earth's surface with multiple vertical layers for the atmosphere and ocean. The state of the atmosphere, land surface, and oceans is updated every time-step, which is typically between 15 minutes and a few hours long. Some fully coupled models, termed Earth System Models (ESM), represent biogeochemical processes involving the carbon and nitrogen cycles, generating feedbacks that modify physical states in the model.

1.2 Why use a GCM?

Weather and climate research is challenging to conduct experimentally due to the inherently large spatial and temporal scales involved. Models driven with input available from satellite observations and surface field measurements allow us to understand our current climate state. A reliable model can also be used to make predictions of how future climate will evolve under different scenarios. Only a fully coupled ESM—that is, a GCM actively simulating atmospheric, oceanic, cryospheric, and land processes feeding information to each other—can explicitly predict climate trends and feedbacks with a high degree of fidelity. These models can assess the behavior of many processes interacting on different temporal and spatial scales, allowing simulation of climate states on the scale of days to centuries.

1.3 Some Limitations of GCMs

Because GCMs represent many processes of the Earth on a grid, they are inherently computationally expensive, and their operation is therefore often limited to supercomputing centers. The utility of a GCM is tied to its spatial and temporal resolution. For example, a model with a timestep of 30 minutes will better predict weather systems and the response to them than one with a timestep of 4 hours, and a land model with a 10 km grid will resolve orography and better predict phenomena such as rain shadows than one that is at a 2 degree grid. However, increasing resolution has a steep cost. A rule of

thumb is that doubling the spatial resolution of an atmospheric GCM will octuple the computational power needed.

The long-known limit of spatial scales is an impediment for two reasons. First, the resolution of model output is too large to be directly applicable to impact studies such as climate effects on regional hydrology. This can be addressed through several downscaling methods [*Mearns et al.*, 2014]. Second, some processes necessary for accurate regional representation in GCMs are smaller than the grid resolution. Localized features such as vegetative or topographical heterogeneity, are necessary to simulate regional behavior. There are also small-scale physical processes such as cloud formation and snowpack metamorphosis. We must represent these sub-grid-scale processes with some form of parameterized behavior. In doing so, we inherently approximate the time or spatial average behavior of these processes. This can be a source of error, and we must weigh the possible uncertainties against the computational costs of explicitly representing them.

Besides those introduced by resolution, uncertainties derived from data can limit the utility of predictive modeling. Observational data sets may be incomplete, are sometimes conflicting, and have their own measurement uncertainties. We are also unsure of the strength and role of feedback mechanisms such as surface albedo, water vapor, and clouds.

1.4 Calculating Radiation in GCMs

The absorption and scattering of radiation occurs on the molecular scale, many orders of magnitude smaller than what can be resolved by climate models. Therefore, modelers

must also parameterize the radiative transfer equations. A common calculation method used by GCMs is the two-stream approximation, due to its computational efficiency. It employs an angular averaged effective flux instead of solving for many angular-dependent intensities, and can account for multiple-scattering phenomena. The delta-Eddington approximation is a particular variant of the two-stream approximation adept at modeling largely forward scattering particles [*Joseph et al.*, 1976]. It is employed in the Community Atmosphere Model (CAM) to model the behavior of clouds and aerosols, and in the Community Land Model (CLM) to represent the snow pack.

1.5 How is the Cryosphere Represented in GCMs?

In an atmosphere at equilibrium, the radiative forcing (RF, units: W m^{-2}) is the change in the top of atmosphere flux resulting from the imposition of a forcing agent. The response, the globally averaged surface temperature change (ΔT, units: K), can be expressed as:

$$\Delta T = \frac{RF}{\gamma} \quad (1)$$

γ (K W^{-1} m^2) is the net climate feedback parameter [*Soden and Held*, 2006]. Note that there is some ambiguity between what an externally imposed forcing agent is and what an internal climate response is. Because of this, we later (i.e., Chapter 2) refer to "radiative effect" where it is not an explicitly external forcing, but rather the radiative influence of a particular component of the climate system. The net feedback is the result of multiple interacting individual feedback mechanisms. Positive feedbacks amplify the strength of a radiative forcing, while negative feedbacks dampen it. Figure 1-1 shows the different

radiative forcings affecting our climate over the age of industrialization. While greenhouse gases exert the largest effect, this work focuses on surface albedo forcing and feedbacks, particularly related to the cryosphere.

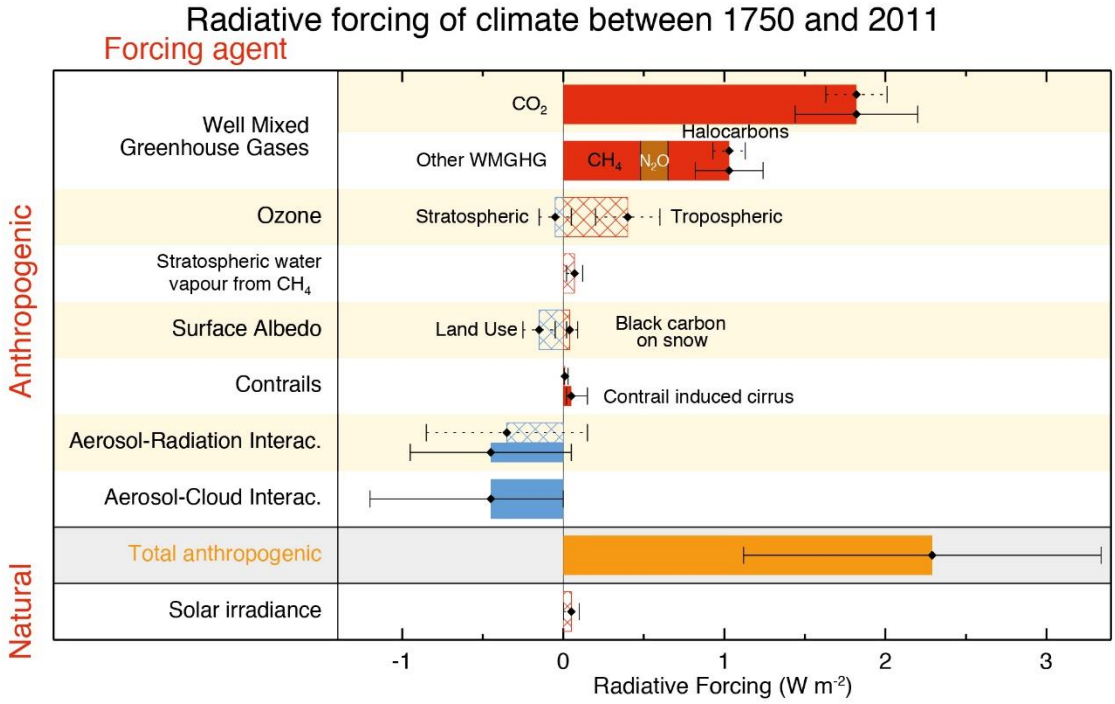

Figure 1-1: Bar chart for RF (hatched) and effective RF (solid) for the period 1750–2011. Uncertainties (5 to 95% confidence range) are given for RF (dotted lines) and ERF (Effective RF, solid lines). Reproduced from Working Group I to the Fifth Assessment Report of the Intergovernmental Panel on Climate Change [*Myhre et al.*, 2013].

The cryosphere (the extent of frozen water in all its forms of snow and ice on Earth's surface) has long been recognized as a large and sensitive influence in climate due to the significant albedo contrast between snow and ice surfaces and the typically darker underlying material, and its large, varying spatial extent. Ice sheets hold the equivalent water of a 66 m sea level rise [*Vaughan et al.*, 2013]. The extent of seasonal snow cover

variation is 29% of the Earth's land surface. Meanwhile, the seasonal variability of Arctic sea ice extent is approximately 10 million square kilometers and variability of Antarctic sea ice is approximately 16 million square kilometers. Seminal works by *Budyko* [1969] and *Sellers* [1969] characterized the albedo influence of large changes in polar ice cap size in simple (for today's standards) one-dimensional models. In *Budyko* [1969], a classic study of the importance of ice albedo feedback, the surface albedo represented that of either ice or ocean, and the received solar radiation was varied accordingly. Warming temperatures caused bright ice to recede to higher latitudes and exposed much darker ocean water, which then absorbed more solar radiation. These studies calculated the critical decrease in radiation that causes a runaway effect. If cooling temperatures cause ice caps to grow beyond a threshold latitude, the world will experience enhanced cooling until it is completely glaciated with bright ice. Then a large enough external increase in radiation would be necessary to re-melt the "snowball Earth". Variations in our planet's orbit over long time periods have been theorized to provide such insolation changes. Termed Milankovitch cycles after scientist Milutin Milankovitch, similar ideas were first proposed in the 19th century by Joseph Adhemar, and later more completely by James Croll. Examination of ocean sediment cores first provided observational evidence supporting a correlation between Milankovitch cycles and ice ages [*Hays et al.*, 1976].

Advances in cryosphere representations in GCMs have been made with the drastic improvement of computational resources. Mass balance of terrestrial snow and marine ice soon followed the early albedo models [*Bryan*, 1969; *Manabe*, 1969; *Bitz and Marshall*, 2012]. Groundwork in glacial rheology formalism [e.g., *Glen*, 1955; *Nye*, 1963] led to computational glacier models in the 1960s-1970s, which later simulated flows of ice

shelves and streams in the 1980s. Numerical sea ice rheology was developed later, but implemented into GCMs at a faster pace [*Bitz and Marshall*, 2012].

In addition to the strongly positive ice albedo feedback and the analogous snow albedo feedback over land, the cryosphere has other feedback mechanisms of concern to modelers. Inherently sensitive to temperature fluctuations, sea ice meltwater affects ocean temperature, density, and circulations. The coupling of marine ice/ocean dynamics remains an area of active model development. Snow, in addition to being highly reflective in the visible spectrum, is an excellent absorber in the infrared [*Wiscombe and Warren*, 1980]. Differences in heat and vapor, as well as kinetic effects, lead to metamorphosis of snow grains as fallen snow ages [*Flanner and Zender*, 2006]. Changes in light scattering behavior of aging snow results in lower albedo. Thus to predict important quantities like snow depth and temperature, a model should incorporate not only shortwave and longwave radiation, but also effects of thermal and vapor diffusion, as well as turbulent energy exchange with the atmosphere. A one-dimensional mass and energy model was created to do just this [*Jordan*, 1991], with similar techniques later incorporated into GCMs.

Modern models have approaches to represent multiple surface types within a single gridcell, i.e., ways to downscale surface processes. Three main methods are: 1) using effective parameters to somehow average over a gridcell, 2) employing probability distribution functions to statistically average quantities, and 3) using a "tile" approach where each tile takes in the same forcing from the atmosphere, and separately computed fluxes are averaged to a gridcell value [*Niu and Zeng*, 2012]. Excellent overviews of how snow albedo can be represented in the presence of differing vegetation appear in *Qu and Hall* [2007] and *Essery* [2013]. The simplest models do not differentiate between

vegetation and ground, and use a weighted average of ground snow and snow-free albedos, depending on how much of the gridcell is covered by vegetation. Slightly more complex models use different albedos for different vegetation categories. Rising further in complexity, there are GCMs where vegetation has snow and snow-free brightness, for different vegetation types. The total albedo is then an average of canopy and ground. At the most complex, there are models that implement a radiative transfer model for the canopy. The Community Land Model is an example of this type, employing a multi-tier "tile" method to represent surface heterogeneity of vegetation and soils in energy and water flux calculations (Figure 1-2). Plant functional types (PFTs) (e.g., boreal needleleaf evergreen tree, C_3 arctic grass, irrigated temperate cereal crop) represent different plant groups with physiological and phenological variables (e.g., monthly leaf area index, canopy height, leaf albedo) derived from observation [*Oleson et al.*, 2013].

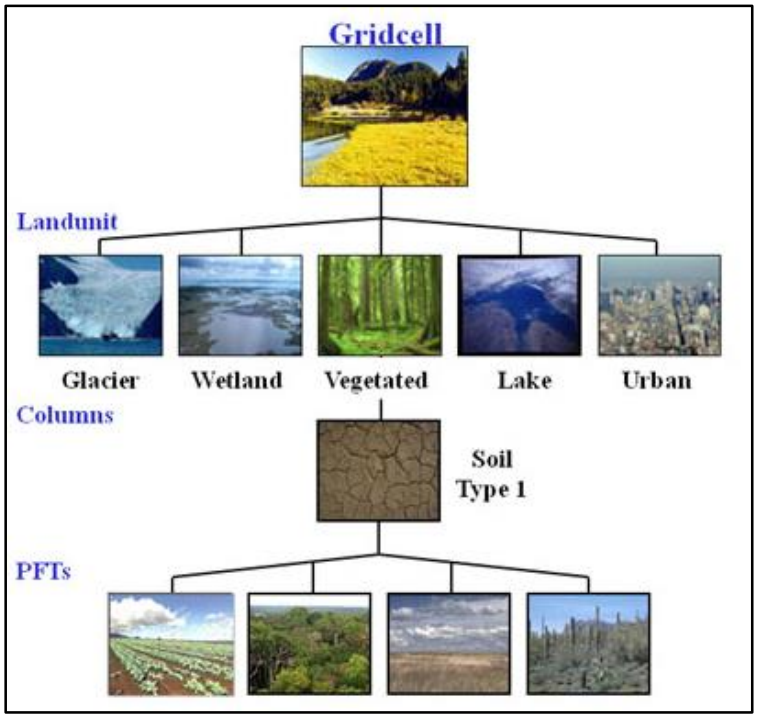

Figure 1-2: A representation of the multi-level "tile" method employed in Community Land Model version 4.0. A gridcell can contain multiple land units. The vegetated landunit can contain separate areas of plant functional types (PFTs). Reproduced from http://www.cesm.ucar.edu/models/clm/surface.heterogeneity.html, accessed 06/28/15.

1.6 Some Present Issues with Radiative Representation of the Cryosphere

1.6.1 Open area snow modeling

Over the last few decades, efforts have been made to compare the fidelity of snow albedo across models. In the late 1990s, there was some limited comparison between standalone snow models [e.g., *Essery et al.*, 1999; *Jin et al.*, 1999; *Schlosser et al.*, 2000; *Boone and Etchevers*, 2001]. A more comprehensive study was undertaken with the Snow Model Intercomparison Project (SnowMIP) [*Fierz et al.*, 2003]. For model validation the

SnowMIP used in-situ observations of snow water equivalent (SWE – the depth of water contained in snowpack if it were melted down), snow depth, run-off, temperature, and albedo. They also quantified the error in snow cover duration, which is of interest not only to hydrology, but also to a radiation perspective. It was found that 65% of the models accurately (within 7 days of snow cover duration error) represented the best-modeled observation site, while only 8% accurately represented the worst one. An analysis was conducted of 21 land surface schemes participating in the Project for the Intercomparison of Land-Surface Parameterization Schemes (PILPS) Phase 2(d) [*Slater et al.*, 2001]. Albedo and fractional snow cover parameterizations were found to have large influences on energy budget. Additionally, model structure such as the link between snow and soil representation resulted in differences in energy partitioning. The influences of parameters such as thermal conductivity, emissivity, and density were also investigated. Most models held high constant (usually 1.0) snow emissivity, yet density, grainsize, and wavelength can influence it in reality. Aged as well as cold snow has been reported to have emissivities in the range 0.80-0.90, suggesting a negative feedback loop with respect to temperature not addressed in these models. Models with snow density employed as a diagnostic variable typically had density-dependent thermal conductivity, snow depth, and snow cover fraction. Large variability in these parameters was noted, but it was not conclusive which would be preferred in global simulations. It was found that ensemble interannual accumulation and ablation behavior were sufficiently represented, but there were significant inter-model variations and weaknesses.

1.6.2 Considering vegetation in snow representations

As snow models have grown more sophisticated and numerous, the representation of vegetated regions has garnered more interest. This is because forest-snow interactions have important effects on Earth's climate, but are more difficult to represent than open areas. The significant amount of land surface covered by forest, and their albedo masking effects, both contribute to their strong influence. Boreal forests in particular cover a significant portion of the Northern Hemisphere's snow-covered area, and exhibit snow presence on the ground for the majority of the year. They have the capacity to intercept about half of snowfall in the canopy, yet they exert a significant albedo masking effect while retaining canopy snow [*Pomeroy et al.*, 1998; *Storck et al.*, 2002; *Essery*, 2013; *Mahat and Tarboton*, 2013]. Additionally, they provide thermal insulation and alter turbulent heat fluxes when compared to short, fully buried vegetation. Multiple sensitivity studies have quantified the snow albedo masking influence these forests have in climate models [*Thomas and Rowntree*, 1992; *Chalita and Le Treut*, 1994; *Douville and Royer*, 1996; *Gallimore and Kutzbach*, 1996; *Betts et al.*, 2001; *Renssen*, 2003].

A follow-up study to the original SnowMIP including several GCM snow schemes focused on the particularly difficult issues with representing snow in forests [*Essery et al.*, 2009]. This not only included albedo masking, but hydrology (through SWE) and energy balance (through soil and surface temperature and radiative fluxes). They noted there was no best fidelity model for all observational sites and years. The presence of under-canopy ground snow was found to be more important to energy balance than the proper quantity of snow. A comparison study evaluating forested mountain snowpack of land surface models found current simulations generally represent seasonal SWE well compare to Snow

Telemetry (SNOTEL) sites, but forest-change experiments revealed differing reasons for this [*Chen et al.,* 2014]. Compared to Ameriflux site measurements, all models overestimated the ratio of outgoing radiation to incoming radiation and underestimated the net ratio of outgoing turbulent heat flux to incoming radiation. Large inter-model discrepancies were found in turbulent fluxes as well as snowmelt and sublimation efficiencies. The analysis highlighted the domino effect snow albedo had on energy budget deficits, temperature, and turbulent energy, and that it was a source of the inter-model variability.

In the context of comparing process-based hydrologic models, an intercomparison framework was developed and used with Western-U.S. watershed case studies [*Clark et al.,* 2015a;2015b]. Physical processes considered included snow albedo, ground snow hydrology, as well as canopy thermodynamics, canopy hydrology, and canopy-influencing turbulence. Comparisons were made of canopy snow interception modeling techniques as well as snow albedo effects on ablation. The study suggests that selecting well-thought parameter values agreeing with in-situ measurements can matter just as much as, or more than, differences in process representation schemes.

1.6.3 Snow radiation biases in the Community Land Model

Among coupled climate models in the Coupled Model Intercomparison Project Phase 3 (CMIP3), snow albedo feedback (SAF) was reported to vary widely, mostly due to the spread in snow cover between models [*Qu and Hall,* 2007]. Models with explicit canopy snow albedo representation generally have lower albedos and thus weaker snow

albedo feedback than observed. An update on the study for Coupled Model Intercomparison Project Phase 5 (CMIP5) found a large spread in SAF persisting in a newer generation of models [*Qu and Hall*, 2014]. The inter-model surface albedo variability was attributed to the drastically different albedo representations of vegetation in snow-affected areas. The boreal forest-occurring zone had the lowest ensemble surface albedo, as well as the greatest variance. This area, along with the Tibetan Plateau and Southern Rocky Mountains, contributes most of the globally-averaged SAF and its variability.

Recent research comparing CMIP3 and CMIP5 models against a multi-observation-derived dataset showed that both generations of models represented SAF reasonably well in the models' ensemble mean, with the important exception of the boreal forest region being biased high, and the Arctic biased low [*Fletcher et al.*, 2015]. The majority of CMIP5 models overestimated the SAF component associated with snow cover fraction change (i.e., from the albedo reduction of removing snow) due to overly bright snow albedo, while underestimating the SAF component associated with snow albedo evolution due to temperatures changes and metamorphosis. In a previous study by the same group, the Community Climate System Model version 4 (CCSM4) was reported to have a North Hemisphere mean spring SAF smaller than observed, due to the smaller–than-observed temperature-albedo component [*Fletcher et al.*, 2012]. The larger-than-observed snow cover component of SAF somewhat compensated for the error.

In another relevant study, the sources of weak CCSM4 SAF in boreal forest regions is investigated [*Thackeray et al.*, 2014]. It was found that the particularly weak SAF in spring stemmed from both overly high midwinter albedo and premature spring decline.

Two parameterization shortfalls in the CCMS4 land model are pinpointed as the causes of these issues. First, no capability exists for vegetation intercepted snow to leave the canopy during freezing temperatures, causing the midwinter bias. Secondly, the radiative influence of the intercepted snow disappears immediately when the temperature rises above the freezing point of water, which is the source of the premature spring albedo decline. Both of these shortcomings stem from the lack of explicit canopy snow hydrology representation. To address this pressing issue, we have developed such a representation based on tower site measurements and remote sensing observations, and integrated it into the land model's radiation scheme.

1.7 GCM Components Employed in the Thesis

Our work primarily focuses on development and application of the Community Earth System Model (CESM), which in various configurations of components can couple the Community Atmosphere Model (CAM), the Community Land Model (CLM), the Community Ice Code (CICE), and the Parallel Ocean Program (POP). Previous versions of CESM employing CAM version 4 are contained within the Community Climate System Model (CCSM4), the predecessor of CESM.

1.8 Outline of the Thesis

In Chapter 2 [*Perket et al.*, 2014] we discuss the framework and creation of the cryosphere radiative effect diagnostic. This instrument is then employed to evaluate inter-model shortwave masking of ice and snow. Additionally, we evaluate the utility of albedo

radiative kernels. Chapter 3 (*Soon to be submitted.*) details the creation and evaluation of an integrated vegetation hydrology-radiation scheme implemented in CLM to combat the discussed snow-affected boreal forest albedo biases. Finally, Chapter 4 (*In preparation*) explores the impacts of the new canopy snow implementation on the simulation of climate under future warming scenarios. Appendix A briefly discusses the generation of albedo radiative kernels, and their utility in inter-model comparisons.

Chapter 2

Cryosphere Radiative Feedback

2.1 Introduction

Realistic portrayal of cryospheric change is critical for accurate climate change modeling. In addition to the strongly positive snow/ice albedo feedback, where increasing temperatures decrease cryospheric coverage, warmer temperatures also darken snow and sea ice through thinning, accelerated metamorphism, and increased melt pond coverage. After cloud and water vapor feedback, surface albedo feedback is the third-strongest global positive feedback mechanism [e.g., *Bony et al.*, 2006; *Soden and Held*, 2006]. Snow area fraction and sea ice extent are important metrics often used to evaluate models, but do not capture the cryospheric radiative influence, which is modulated by factors such as seasonal insolation, cloudiness, vegetation cover, ground albedo, melt pond distribution, and impurity content in snow.

To quantify these influences, we incorporate a new diagnostic into the Community Earth System Model (CESM): the cryosphere radiative effect (CrRE). CESM includes sophisticated snow and sea ice physics, making it a suitable candidate for such development. The ice model includes ponding and multiple sub-grid ice thickness categories, while the multi-layer snow model accounts for metamorphosis, compaction, and vegetation burial [*Lawrence et al.*, 2011; *Holland et al.*, 2012] Both models apply two-

stream radiative transfer models to calculate albedo and account for embedded light-absorbing aerosols [*Briegleb and Light,* 2007; *Flanner et al.*, 2007].

Analogous to the cloud radiative effect [e.g., *Ramanathan et al.*, 1989; *Arking*, 1991; *Stephens*, 2005], CrRE is defined as the instantaneous influence of surface snow and sea ice on the top-of-model (TOM) shortwave energy budget [*Flanner et al.*, 2011], TOM being nearly equivalent to the top of the atmosphere. CrRE incorporates the influences of vegetation masking and sea ice ponding on albedo, as well as insolation variation and shortwave attenuation and scattering by clouds, aerosols, and gases. Longwave cryospheric effects are not included here, though they may also be important. Although broadband emissivities of cryospheric and non-cryospheric surfaces are similar, snow and ice can insulate the ground or facilitate substantial cooling of the skin surface, thereby reducing outgoing longwave radiation. Estimation of longwave effects, however, requires calculation of temperature feedback in the absence of snow, and thus cannot be accomplished through an instantaneous framework.

In addition to providing the exact shortwave influence of the cryosphere, the CrRE diagnostic can be used to evaluate the accuracy of assumptions applied in surface albedo feedback analysis. For example, the radiative kernel method has been applied in several analyses of albedo feedback [e.g., *Shell et al.*, 2008; *Soden et al.*, 2008; *Donohoe and Battisti*, 2011; *Flanner et al.*, 2011; *Qu and Hall*, 2013], but the importance of consistency between atmospheric fields used to generate kernels and non-linearities in top-of-atmosphere flux change with albedo changes larger than 0.01 (the typical perturbation) have not been rigorously evaluated.

2.2 Diagnostic CrRE calculation

We implemented the diagnostic CrRE calculations in CESM versions 1.0.5 and 1.1.1 [*Gent et al.*, 2011; *Hurrell et al.*, 2013]. CESM contains the Community Land Model (CLM), the Community Ice Code (CICE) model, the Parallel Ocean Program (POP), and the Community Atmosphere Model (CAM), among other components, synchronized through a coupler. CrRE was calculated by extracting, at each time step, snow-free albedo from CLM and ice-free ocean albedo from CICE, passing these states through the coupler (CPL) to the atmosphere model, and conducting parallel atmospheric radiative transfer calculations with the true and cryosphere-free surface albedos (Figure 2-1). The difference in TOM net shortwave flux between these calculations provides the cryosphere radiative

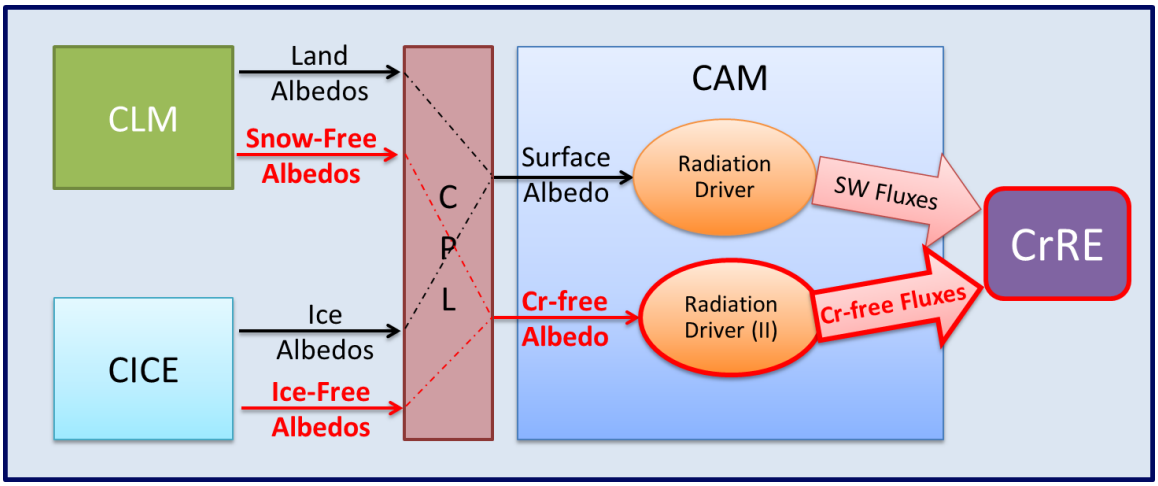

Figure 2-1: Diagram of CrRE computation. CLM, CICE, and CAM are CESM's land, sea ice, and atmosphere models respectively, while CPL is the coupler software connecting component models. Additions to the CESM code are highlighted in red.

effect. Note that open-ocean albedo is calculated by default in the coupler, not POP. When sea ice is present, CICE computes albedo. For the purposes of CrRE, we incorporated this open-water albedo formalism into CICE, identical to how CESM would treat ice-free ocean. CESM partitions surface albedo into four components: direct visible, diffuse visible,

direct near-IR, and diffuse near-IR. Merging of land, ocean, and sea ice albedos is handled consistently for both sets of surfaces. Over glaciers and ice-sheets, CrRE represents the influence of overlying snow relative to bare ice, which in CESM has constant visible and near-IR albedos of 0.80 and 0.55, respectively. This diagnostic therefore offers a description of the fast-feedback (snow and sea ice) component of the cryosphere. While ice sheets clearly provide large capacity for altering planetary albedo over long timescales, estimation of their radiative influence requires involved assumptions of how the ice sheet-free albedo is related to vegetation cover, isostatic rebound, and sea-level.

2.3 Model Simulations

We conducted two fully-coupled 21st century simulations driven by the RCP8.5 forcing scenario with the CrRE diagnostic enabled, using CAM4 in CESM 1.0.5 (i.e., CCSM4; using the B_RCP8.5_CN component set) and CAM5 in CESM 1.1.1 (B_RCP8.5_CAM5_CN component set) [*Meinshausen et al.*, 2011]. These hybrid runs used year 2007 initial conditions from existing RCP8.5 experiments, and progressed to year 2100. This allowed us to evaluate evolution of snow and ice radiative influence in response to strong warming, simulated by different model versions. We also conducted 10-year present-day simulations (B_2000_CN component set) with CAM4 physics in CESM 1.0.5 and CAM5 in CESM 1.1.1 for comparison with observationally derived estimates of CrRE. These runs were allowed a one-year spin-up period before data were taken for analysis. All simulations were conducted at 0.9x1.25 degree horizontal resolution.

2.4 Observationally Derived CrRE

We apply observation-based CrRE data from *Flanner et al.* [2011]. This data set is derived from a variety of remote sensing measurements and consists of monthly-resolved 1x1 degree resolution Northern Hemisphere (NH) CrRE during 1979-2008. We re-derived the observation-based data with two key changes that facilitate a more direct comparison with model output. First, we assume the same snow-free albedos over ice sheets and glaciers as used in CLM. Second, we replace the surface albedo radiative kernels used by *Flanner et al.* [2011] with newly-created kernels generated from CCSM4 and CESM1-CAM5, providing consistent cloud conditions for evaluating cryospheric influences from these two models. Kernels were generated using the instantaneous TOM flux changes associated with a +0.01 perturbation in surface albedo, consistent with the method applied by *Shell et al.* [2008]. The methodology is provided in Appendix A.

2.5 Present Day CrRE

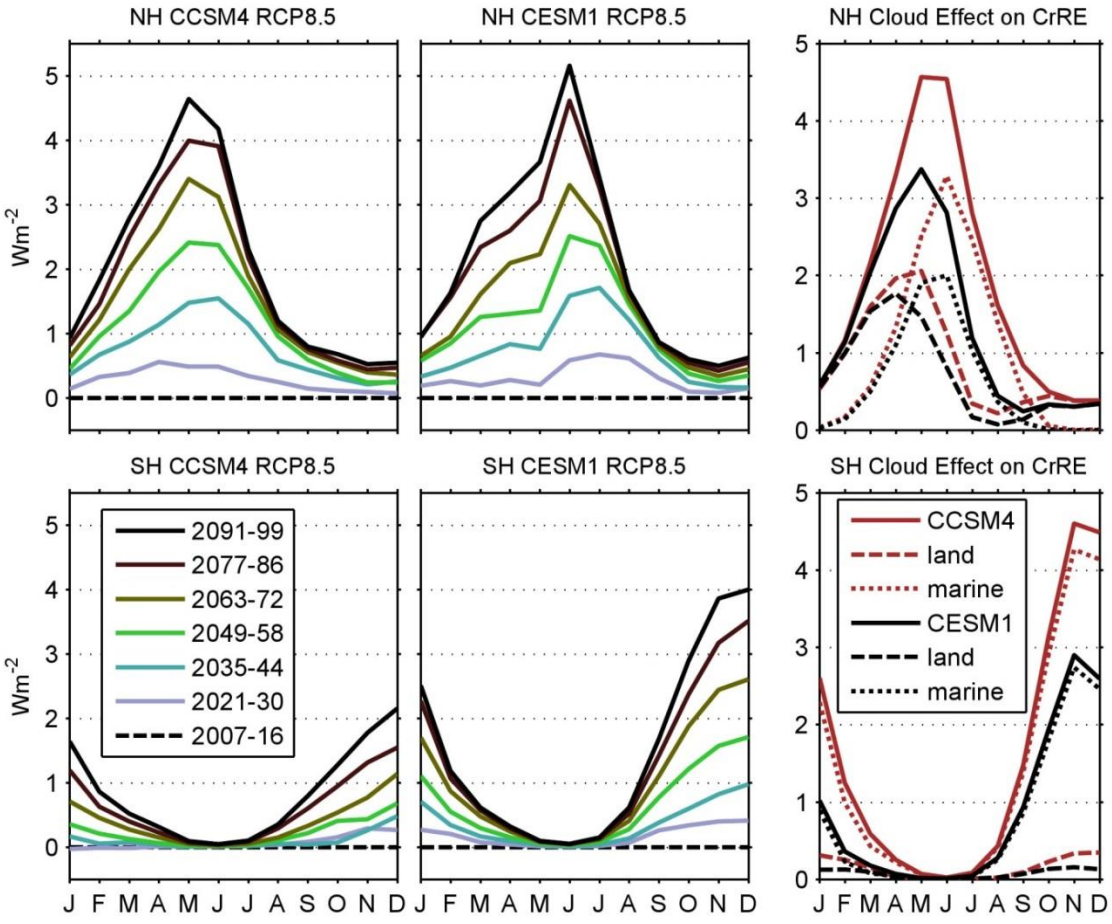

Figure 2-2: Multi-decadal change in Northern (top) and Southern (bottom) Hemisphere all-sky CrRE simulated in the CCSM4 (left) and CESM1-CAM5 (middle) models under the RCP 8.5 Scenario. The mean of years 2007-2016 is used as the baseline and subtracted from ten year averages over different periods. On right are cloud effects on present-day CrRE (all-sky - clear-sky conditions) partitioned into total, land, and marine components. Positive numbers indicate CrRE has become less negative.

In the present day simulations, global annual clear-sky CrRE is -5.7±0.07 W m^{-2} in CCSM4 and -4.9±0.08 W m^{-2} in CESM1-CAM5 (Table 2-1). In CCSM4 and CESM1, the clear-sky conditions remove the influence of clouds, while including aerosols and gases. The spread represents the interannual standard deviation for each model run. The difference between models is due largely to greater SH sea ice cover in CCSM4. The all-sky CrRE in

both models is -3.8 (±0.05 in CCSM4 and ±0.06 in CESM1-CAM5) W m^{-2}, with the similar magnitudes resulting from greater cloud masking of cryospheric regions in CCSM4 than CESM1-CAM5 (Figure 2-2). Seasonal variation in CrRE is strongly influenced by the insolation cycle in each hemisphere, with peak NH and SH CrRE occurring in May and November, respectively (Figure 2-3), about two months after peak

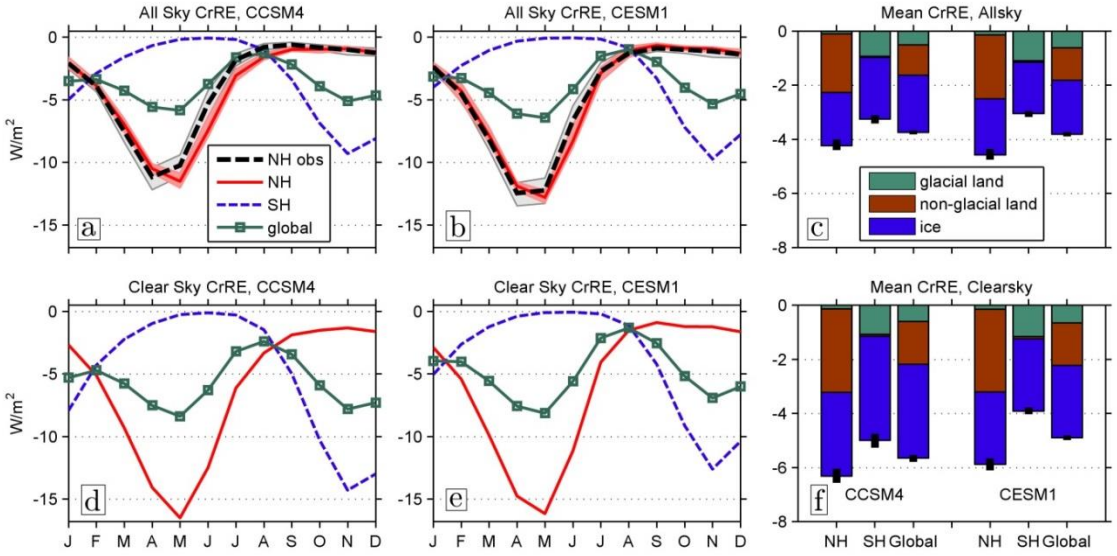

Figure 2-3: Present-day CrRE components simulated with CCSM4 (left, a & d) and CESM1-CAM5 (middle, b & e), for all sky conditions (top row) and clear-sky conditions (bottom row). Northern Hemisphere (NH) observation-based CrRE from *Flanner et al.* [2011] recalculated using a CAM4 (a) and CAM5 (b) radiative kernel are also shown. Shading in (a) and (b) indicates full ranges of the NH CrRE in each month. Black bars in (c) and (f) indicate full range of annual-mean CrRE.

sea ice extent and 3-4 months after peak snow extent. Sea ice tends to cause the largest effect per unit area due to the darkness of ocean water, and contributes 57% and 52% of global all-sky CrRE in CCSM4 and CESM1-CAM5, respectively (Table 2-1). Snow cover over non-glacial areas contributes 30% and 32% of the global effect in these two models, almost all of it from the Northern Hemisphere. The smaller albedo difference between snow and permanent glaciers results in only 14% and 16% of the effect originating from

supra-glacial snow (snow atop ice sheets and glaciers), mostly from Antarctica. Total CrRE is larger in the SH, with the majority of SH effect originating from sea ice, whereas NH CrRE is partitioned nearly evenly between snow and sea ice (Table 2-1). SH supra-glacial snow and sea ice contributions are 15% smaller (less negative) and 20% larger (more negative), respectively, in CCSM4 compared with CESM1-CAM5 (Table 2-1).

Global annual present day NH model and observation-based CrRE compare well with both CCSM4 and CESM1-CAM5 treatment (Figure 2-3: a,b). Using the new CAM4 and CAM5 radiative kernels, annual observationally-derived means are -3.9 and -4.6 W m^{-2}, demonstrating influence of different cloud treatments on CrRE. NH model means are larger by 10% and 1% of observation for CCSM4 and CESM1-CAM5, respectively. The high bias in CCSM4 CrRE occurs during March-September, and is caused by excessive sea ice. In both models CrRE is more negative than observations over Greenland, the Canadian Arctic Archipelago and most of the Tibetan Plateau, and is less negative over parts of central-eastern Canada and small regions west of the Tibetan Plateau (Figure 2-4: e,f). Overly reflective snow on ice sheets, excessive snow cover on the

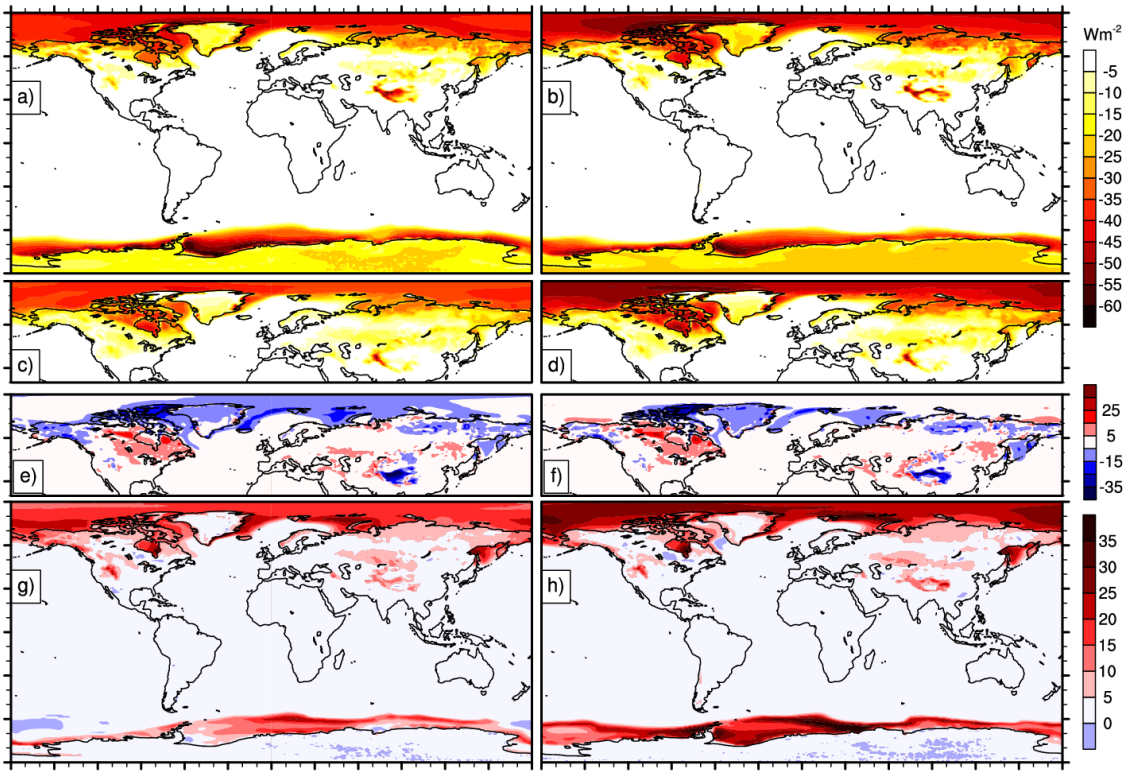

Figure 2-4: Present day CrRE simulated using CCSM4 (a) and CESM1-CAM5 (b), along with Northern Hemisphere observations rederived from *Flanner et al.* [2011] using a CAM4 radiative kernel (c) and a CAM5 kernel (d). Model results subtracted by observation are shown in (e) and (f). Differences between the means of periods 2090-2099 and 2007-2016 of the RCP 8.5 simulations are shown in g) and h).

Tibetan Plateau, and excessive sea ice in the North Atlantic may explain some of these discrepancies. The contribution of snow may be underestimated over glacial regions, however, because of a higher bare ice albedo assumed in CLM than measured in the ablation zones of Greenland [*Bøggild et al.*, 2010; *Box et al.*, 2012]. Moreover, darkening of snow-free ice surfaces through increased water content is not treated in our modeling, but constitutes a fast feedback component of cryospheric albedo change.

Global CrRE increases by 51% in clear-sky conditions compared to all-sky in CCSM4, and by 29% in CESM1-CAM5 (Figure 2-3, comparing c and f). Cloud masking

on CrRE is largest over sea ice (63% and 35% clear-sky increases in the respective models) and smallest over glacial land (17% and 6% increases). Low Arctic clouds increase automatically with sea ice melting in CAM4 due to a cloud parameterization designed for lower latitudes, resulting in incorrect cloud response to ice melting [*Kay et al.*, 2011]. Additionally, clouds in this region are known to be too optically thick in CAM4 and too thin in CAM5 [*Kay et al.*, 2012]. These factors result in unrealistic Arctic cloud masking, which also is expected over Antarctic sea ice. Clouds shield cryospheric influence to a lesser extent in these models than the masking of surface albedo anomalies found in previous studies that applied radiative kernels derived from older climate models [*Donohoe and Battisti*, 2011; *Flanner et al.*, 2011; *Qu and Hall*, 2014].

CrRE was also evaluated at the surface. Under all-sky conditions, the cryosphere has the effect of increasing global annual surface downwelling solar flux by 1.2±0.02 and 0.9±0.02 Wm^{-2} in CCSM4 and CESM1-CAM5, respectively, due to multiple scattering between clouds and the surface. Under clear-sky conditions, both models' downwelling shortwave flux rise by 0.4±0.01 W m^{-2} due to Rayleigh scattering and surface cryosphere albedo.

2.6 21st Century Evolution of CrRE

We now examine 21st century CrRE changes under the RCP 8.5 forcing scenario. Equilibrium climate sensitivity and 21st century climate response is greater in CESM1-CAM5 compared to CCSM4 [*Meehl et al.*, 2013]. The global mean instantaneous shortwave influence of the cryosphere diminishes in magnitude (becoming less negative) by 1.4±0.1 W m^{-2} during the 21st century (mean of years 2090-2099 relative to years 2007-

2016) in the CCSM4 experiment, and by 1.8±0.1 Wm^{-2} in CESM1-CAM5 (Figure 2-5, Table 2-1), or by 38% and 46% of the initial 21st century effect. The boreal land snow,

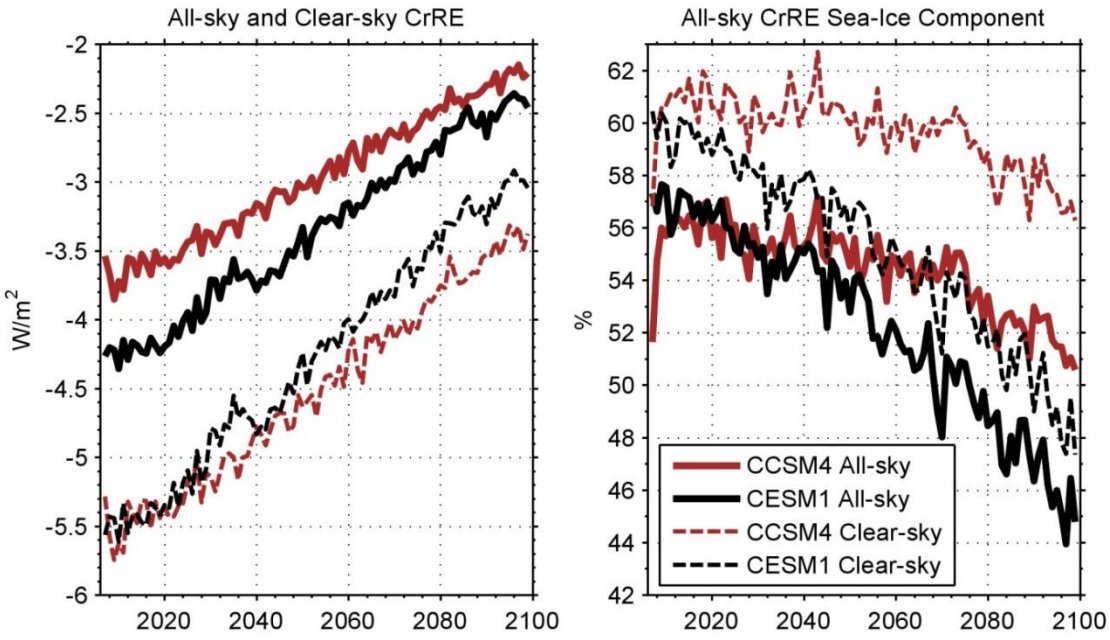

Figure 2-5: Global annual averages of the all-sky and clear-sky CrRE simulated with CCSM4 and CESM1-CAM5, forced with the RCP 8.5 scenario. The right panel shows the portion of CrRE produced by the presence of sea ice.

boreal sea ice, and austral sea ice components each contribute between 0.4-0.7 W m^{-2} to global CrRE diminishment in both models. Changes are largest around the summer solstice for each hemisphere (Figure 2-2, left). The resulting increases in planetary absorbed energy are about 24-31% as large as the change in anthropogenic radiative forcing during this period (5.7 W m^{-2}) for the RCP8.5 scenario [*Meinshausen et al.*, 2011]. The changes in all-sky and clear-sky CrRE remain mostly steady throughout the 21st century in both the North and South Hemispheres (Figure 2-5, left), though marine CrRE contribution diminishes more rapidly than terrestrial as sea ice is lost (Figure 2-5, right). Early 21st century CrRE is more negative in the CESM1-CAM5 RCP 8.5 simulation than in the present-day control

simulation (Table 2-1), caused by differences in shortwave cloud forcing and ice area. Initial CrRE in the CESM1-CAM5 RCP8.5 experiment is also more negative than the CCSM4 version, providing a larger capacity for 21st century change. Under clear-sky conditions, the CCSM4 and CESM1-CAM5 21st century CrRE changes are +2.0 and +2.4 W m^{-2}.

		Present-day				**21st Century RCP 8.5[b]**		
Model Version	Region	Total	Glacial Land	Sea ice	Non-Glacial Land	Total	Land	Sea ice
CCSM4	NH	4.2 (6.3)	0.1 (0.1)	2.0 (3.1)	2.2 (3.1)	4.1/2.1 (6.1/3.3)	2.3/1.3 (3.2/1.9)	1.8/0.8 (2.9/1.4)
	SH	3.3 (5.0)	0.9 (1.1)	2.3 (3.9)	0.0 (0.1)	3.2/2.4 (4.9/3.6)	1.0/0.9 (1.2/1.1)	2.2/1.5 (3.7/2.5)
	Global	3.8 (5.7)	0.5 (0.6)	2.1 (3.5)	1.1 (1.6)	3.6/2.2 (5.5/3.4)	1.6/1.1 (2.2/1.5)	2.0/1.2 (3.3/2.0)
CESM1-CAM5	NH	4.6 (5.9)	0.1 (0.2)	2.1 (2.7)	2.4 (3.1)	4.7/2.7 (6.0/3.3)	2.5/1.6 (3.2/2.0)	2.3/1.1 (2.9/1.3)
	SH	3.1 (3.9)	1.1 (1.2)	1.9 (2.7)	0.1 (0.1)	3.7/2.2 (4.9/2.8)	1.2/1.1 (1.3/1.2)	2.6/1.2 (3.6/1.7)
	Global	3.8 (4.9)	0.6 (0.7)	2.0 (2.7)	1.2 (1.6)	4.2/2.5 (5.5/3.1)	1.8/1.3 (2.2/1.6)	2.4/1.1 (3.3/1.5)

[a]All values are negative. Numbers in parenthesis are clear-sky CrRE.

[b]Pairs are [mean of years 2007-2016] / [mean of years 2090-2099].

Table 2-1: All- and Clear-sky Cryosphere Radiative Effect (W m^{-2})

Incorporating global surface temperature change enables an assessment of the global cryospheric albedo feedback, which we find to be +0.41±0.06 W m^{-2} K^{-1} in CCSM4 and +0.45±0.04 W m^{-2} K^{-1} in CESM1-CAM5. These feedbacks are slightly stronger than

the 21st-century multi-model mean global albedo feedback of +0.3±0.09 W m^{-2} K^{-1} found by *Winton* [2006] from twelve models used in the Intergovernmental Panel on Climate Change fourth assessment report, but NH cryosphere albedo feedbacks (+0.46±0.04 and 0.47±0.07 W m^{-2} K^{-1}) are smaller than the 30-year NH feedback of +0.6 W m^{-2} K^{-1} derived from observations during 1979-2008 [*Flanner et al.*, 2011]. Though CESM1-CAM5 has a 29% larger CrRE change over the RCP8.5 experiment than CCSM4, it only has a 10% greater cryospheric feedback, reflecting the larger climate response in CESM1-CAM5.

2.7 Conclusions

We implement a new diagnostic calculation in CESM of the shortwave cryosphere radiative effect (CrRE), or the exact, instantaneous influence of snow and sea ice on Earth's solar radiation budget. Present-day simulations show that rapidly-evolving cryospheric components diminish TOM net solar energy flux by 3.8 W m^{-2} globally, and by 4.2-4.6 W m^{-2} in the Northern Hemisphere, in good agreement with observational assessments. However, CCSM4 exhibits the compensating effects of larger sea ice extent and larger cloud masking of cryospheric surfaces than CESM1-CAM5. CrRE is strongly influenced by the seasonal insolation cycle, and sea ice contributes more to CrRE than terrestrial seasonal snow or glaciers in the present climate. Diminishing cryospheric cover causes global CrRE to decrease (become less negative) by 1.4 and 1.8 W m^{-2}, respectively, in CCSM4 and CESM1-CAM5 RCP8.5 simulations between the beginning and end of the 21st century. Global cryospheric albedo feedbacks are +0.41 and +0.45 W m^{-2} K^{-1}, indicating that the two models exhibit similar temperature-normalized CrRE change.

Chapter 3

Reducing CLM Albedo Biases in Snow-Effected Forests with Improved Canopy Interception Scheme

3.1 Introduction

The handling of interactions between snow and vegetation in the Northern Hemisphere has been identified as an imperative area for global climate model improvement in order to assess climate impacts [*Essery*, 2013]. A large snow albedo feedback range was found between simulations in the Coupled Model Intercomparison Project version 3 (CMIP3), and the issue continued to be present in CMIP5 [*Qu and Hall*, 2014]. This variability largely contributes to current uncertainty in North Hemisphere land surface warming predictions, and particularly large deviations in boreal forest. Boreal forest representation in particular has both a large inter-model spread in albedo and model bias during snowy months. The importance of this region comes from occupying a significant portion of Northern Hemisphere (NH) snow-covered area, exhibiting snow presence on the ground for the majority of the year, and having the capacity to intercept about half of snowfall in the canopy yet maintaining lower albedo than snow-covered ground [*Pomeroy et al.*, 1998; *Storck et al.*, 2002; *Essery*, 2013; *Mahat and Tarboton*, 2013]. The boreal forests zone is the source of much of the inter-model feedback variability in CMIP5 models [*Qu and Hall*, 2014], with a high ensemble mean bias in the region compared to multi-sourced observational dataset [*Fletcher et al.*, 2015]. This region is

currently experiencing enhanced warming due to surface darkening including woody vegetation spreading northward, existing vegetation in the region thickening, and reduced snow extent and duration [*Loranty et al.*, 2014].

There are substantial discrepancies in the modeling of forested area snow physics [*Feng et al.*, 2008; *Essery et al.*, 2009; *Chen et al.*, 2014]. There exists a large variance between land surface models mainly due to the inability to correctly represent forested snow albedo [*Chen et al.*, 2014]. These albedo biases have cascading effects on surface temperature, energy budget deficits, and turbulent fluxes. A number of surface models overestimate albedo in snow-effected forest areas compared to remote sensing and tower measurements [*Chen et al.*, 2014].

CLM is the land surface model for the Community Earth System Model (CESM), a fully-coupled global climate model. It represents vegetation canopy with radiation and precipitation processes computed separately from the rest of the surface. Shortwave and longwave radiation from the canopy to the atmosphere and ground are calculated, as well as evapo-transpiration moisture and energy fluxes. The model also accounts for precipitation throughfall and some interception. However the canopy model does not distinguish between intercepted liquid and frozen phases. There is no explicit vegetation snow storage, and hence no method to link captured snow and albedo in the CLM radiation scheme. This contributes significantly to albedo biases compared to satellite observations. Particularly, lack of canopy snow unloading processes contributes to overly high mid-winter albedo, and a hard-wired dependence of vegetation albedo on temperature [*Thackeray et al.*, 2014]. Representation of surface albedo considerably alters climate in the CLM [*Lawrence and Chase*, 2007]. We seek to rectify these issues by integrating

explicit canopy intercepted snow storage into CLM, and linking this to the albedo representation.

3.2 Methods – Model Development

Our general approach for improving canopy snow hydrology and albedo in CLM is as follows. Initial hydrology modifications to CLM vegetation were evaluated by comparing single-column simulations against field canopy snow interception measurements, and were adjusted to ensure appropriate model representation of accumulated snow mass and retention rates on model time-step scales. With a more representative canopy hydrology scheme in hand, the modifications were integrated with an adjusted radiation scheme. Albedo in global simulations were compared to MODIS product MCD43C3, collection 5 visible black-sky albedo [*Schaaf et al.*, 2002]. The influence of intercepted snow mass on canopy optical parameters was adjusted to observations until a base configuration was arrived at that provided improved albedo behavior both globally but especially in boreal-forest dominated regions. A sensitivity study followed, where several parameters were individually adjusted, leading to an albedo-optimized configuration that prioritizes cumulative gridcell error reduction in surface albedo.

3.2.1 Hydrology

New modifications include separate storage terms for liquid and solid phases of H_2O, each with unique maximum capacities (Figure 3-1). Liquid capacity is limited to the current

model water capacity, and snow capacity is set to a larger multiple of combined

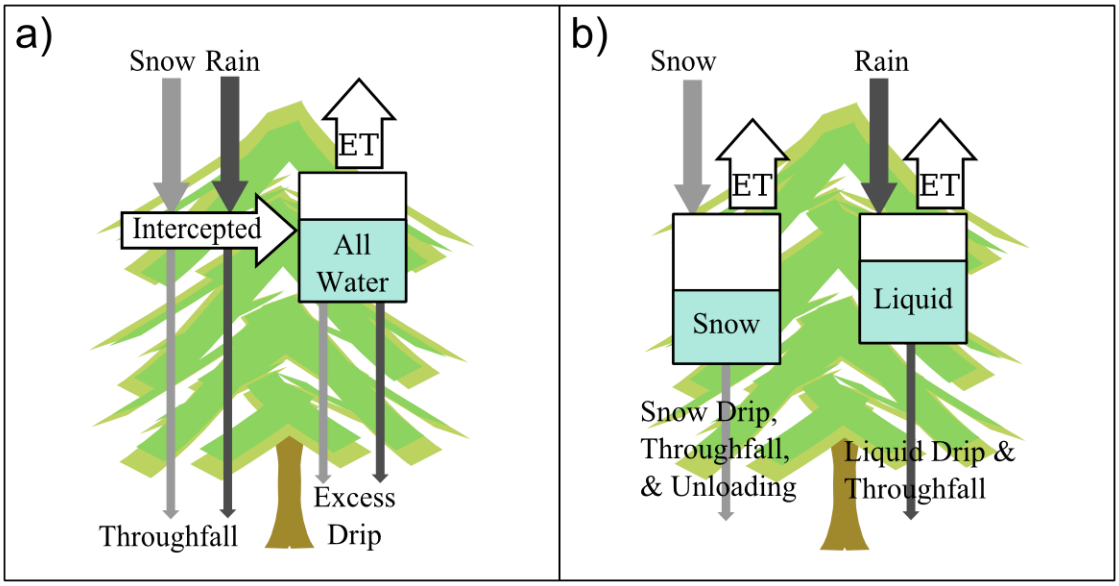

Figure 3-1: Diagram of unmodified (a) and new (b) CLM canopy precipitation treatment.

leaf and stem area indices. Snow unloading fluxes have also been incorporated, providing a pathway for snow transfer from canopy to ground. There are unloading fluxes representing both wind-blown and temperature-based sliding and melt events, based on observation-derived e-folding times from *Roesch* [2001]. The interception rate of snow was separated from that of rain. In unmodified CLM 4.5, the total canopy water storage change due to precipitation interception in a time-step is (kg m^{-2}):

$$\Delta W^{intr} = 0.25(q_{rain} + q_{snow})(1 - e^{-0.5(LAI+SAI)}) \cdot \Delta t. \quad (2)$$

q_{rain} and q_{snow} are the precipitation rates (kg m^{-2} s^{-1}) for rain and snow, LAI and SAI are the leaf and stem area indices, and Δt is the model time-step. The new total interception rate becomes the sum of the following phase-separated snow and liquid contributions:

$$\Delta W_{snow}^{intr} = (c_1 \cdot q_{snow})(1 - e^{-0.5(LAI+SAI)})\Delta t, \quad (3)$$

$$\Delta W_{liquid}^{intr} = (0.25 \cdot q_{rain})(1 - e^{-0.5(LAI+SAI)})\Delta t. \quad (4)$$

A value of c_1=1.0 reflects the reality that a leaf can store more snow than liquid water, departing from a value of 0.25 for all water regardless of phase in the existing model [*Lawrence et al.*, 2007]. In unmodified CLM 4.5, storage is limited to a maximum capacity of:

$$W_{max} = \left(0.1 \ \frac{kg}{m^2}\right)(LAI + SAI). \quad (5)$$

If in a time-step,$(W + \Delta W^{intr}) > W_{max}$, the excess is removed from canopy storage and transferred to the ground via drip fluxes (kg m^{-2} s^{-1}):

$$q_{liquid}^{drip} = \frac{W+\Delta W^{intr}-W_{max}}{\Delta t}\frac{q_{rain}}{q_{rain}+q_{snow}}, \quad (6)$$

$$q_{snow}^{drip} = \frac{W+\Delta W^{intr}-W_{max}}{\Delta t}\frac{q_{snow}}{q_{rain}+q_{snow}}. \quad (7)$$

The division between drip phases is dependent on the current time-step precipitation. Our new modifications separate the storage maximums $W_{max}^{snow}$and W_{max}^{liq} (Figure 3-1). The new drip fluxes become:

$$q_{liquid}^{drip} = \frac{W+\Delta W_{liquid}^{intr}-W_{max}^{liq}}{\Delta t}, \quad (8)$$

$$q_{snow}^{drip} = \frac{W+\Delta W_{snow}^{intr}-W_{max}^{snow}}{\Delta t}. \quad (9)$$

This removes the dependence on current precipitation type, and allows the model to utilize new phase storage quantities to determine drip. CLM now has a "memory" of canopy

accumulation phase. The total water removed from the canopy during a time-step via evapotranspiration fluxes ($q_{veg}^{trans}$and q_{veg}^{evap}) is:

$$\Delta W^{ET} = \left(q_{veg}^{trans} + q_{veg}^{evap}\right)\Delta t. \quad (10)$$

In the modified model this is taken from the appropriate canopy reservoir depending on vegetation temperature T_{veg} and availability of water stores:

$$\begin{aligned} \Delta W_{liquid}^{ET} &= \Delta W^{ET} && , T_{veg} > 0°C \\ \Delta W_{snow}^{ET} &= \Delta W^{ET} - W_{liquid} && , T_{veg} > 0°C, \ \Delta W^{ET} > W_{liq}, \end{aligned} \quad (11)$$

$$\begin{aligned} \Delta W_{snow}^{ET} &= \Delta W^{ET} && , T_{veg} < 0°C \\ \Delta W_{liquid}^{ET} &= \Delta W^{ET} - W_{snow} && , T_{veg} < 0°C, \ \Delta W^{ET} > W_{snow}. \end{aligned} \quad (12)$$

Canopy snow sliding events from wind and warming temperatures were modeled from linear fluxes and e-folding times from *Roesch et al.* [2001]. The influence of these fluxes on canopy snow storage can be expressed as:

$$\Delta W_{snow}^{unload} = (q_{wind} + q_{temp})\Delta t. \quad (13)$$

In Eq. (13), ΔW_{snow}^{unload} (kg m^{-2}) is the change in snow storage in a model time step Δt, q_{wind} is the unloading flux due to windspeed u (m s^{-1}), and q_{temp} (kg m^{-2} s^{-1}) is the canopy unloading due to melt and sliding events at temperature T (K) :

$$q_{wind} = W_{snow} u / c_2, \quad (14)$$

$$q_{temp} = \max\{0, W_{snow}(T - 270\ K)/c_3\}. \quad (15)$$

With these modifications, CLM 4.5 conducted in single-point mode with 30 minute time-step was compared with mature needleleaf evergreen canopy snow mass measurements collected in the Umpqua Forest, Oregon as described by *Storck* [2002] and *Andreadis et al.*, [2009]. Atmospheric conditions taken concurrently with the tree weighings from a nearby shelterwood site were employed as model forcing. Intercepted snow load measurements for cut trees were measured continuously for several winters in the study with lysimeters. A pattern of rapid accumulation followed by rapid unloading for individual snowfall events was observed (shown in next section). The largest sublimation event reported was 4.3 mm over 7 hours, but it was noted such occurrences were rare because of the limited time that accumulated snow was retained in the canopy. The average sublimation rate over a season was less than 1 mm/day, while melt drip and snow mass release constituted the majority of canopy snow removal. It was estimated that 70% of remaining snow removal in this warm maritime climate was from melt drip and 30% from solid snow unloading. Comparisons with the 1996-1997 and 1997-1998 winter seasons were made in this study.

The liquid maximum was kept to the unmodified model's total maximum (meant for small amounts of rain and dew):

$$W_{\max}^{\mathrm{liq}} = (0.1\ \mathrm{kg\ m^{-2}\ s^{-1}})(\mathrm{LAI} + \mathrm{SAI}). \tag{16}$$

The newly-created maximum snow storage capacity with adjustable parameter c_4 is:

$$W_{\max}^{\mathrm{snow}} = (c_4\ \mathrm{kg\ m^{-2}})(\mathrm{LAI} + \mathrm{SAI}). \tag{17}$$

From reference to *Roesch et al.*, [2001] and evaluation of CLM with the 2 seasons of Umpqua forest data, the unload constants $c_2 = 9.35\text{x}10^4$ (m) and $c_3 = 1.56\text{x}10^5$ (K s) were selected for the base configuration. The maximum snow storage constant c_4 was chosen to be 6.0. This is consistent with field measurements and needleleaf evergreen interception maximums as reported in *Pomeroy et al.*, [1998]. These selections provided good agreement of the model with the intercepted snow magnitude and timing of the observations (Figure 3-2). The total result is a simplistic representation of snow interception during and after precipitation events in the style of existing CLM hydrology.

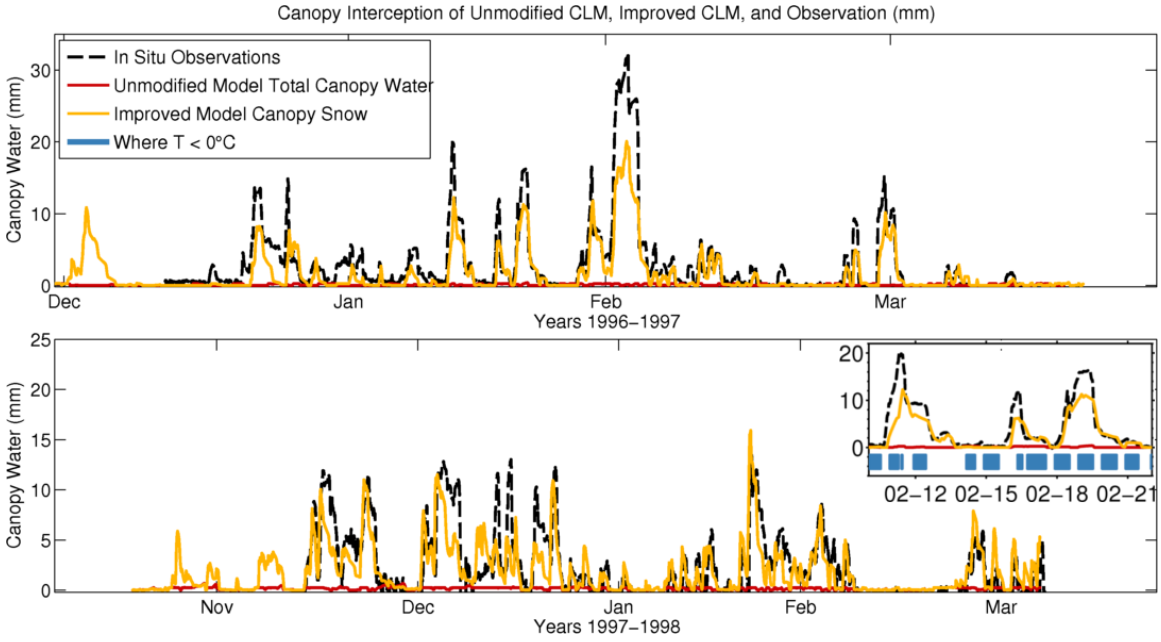

Figure 3-2: Obervational Umpqua Forest canopy intercepted snow water equivalent for two winters as published in *Storck*, [2002], overlayed with unoddified and improved (base configuration) CLM interception using concurrent site conditions as atmospheric forcing. Inset shows a portion of February 1997 in detail. Regions with blue bars indicate when model vegetation temperature is below the freezing point of water, where unmodified CLM represents canopy water as having snow optical properties.

3.2.2 Radiation

The improved canopy hydrology was then integrated with the CLM two steam approximation radiative transfer scheme, detailed by *Oleson et al.*, [2013]. In the unmodified model optical parameters are linear combinations of vegetation and snow values below freezing temperatures, weighted by wetted leaf fraction (as shown for single-scatter albedo parameter ω in Eq. (18).

$$\omega = \begin{cases} \omega_{\text{leaf}}, & T_{\text{veg}} > 0°\text{C} \\ (1 - f_{\text{wet}})\omega_{\text{leaf}} + f_{\text{wet}}\omega^{\text{snow}}_{\text{leaf}}, & T_{\text{veg}} < 0°\text{C} \end{cases} \tag{18}$$

New radiation treatment (Eq. (19)) removes explicit temperature dependence by replacing wetted canopy fraction (f_{wet}) with canopy intercepted snow fraction (f_{cansnow}).

$$\omega = (1 - f_{\text{cansnow}})\omega_{\text{leaf}} + f_{\text{cansnow}}\omega^{\text{snow}}_{\text{leaf}} \tag{19}$$

The unmodified model employs f_{wet} as shown in Eq. (20), where W is the stored total canopy water.

$$f_{\text{wet}} = (W/W_{\text{max}})^{2/3} \tag{20}$$

This nonlinearity ensures realistic evapotranspiration rates off the vegetation [*Deardorff*, 1978]. In freezing temperatures, it ensures a more quickly brightening canopy than a linear relationship for small amounts of water. We found this advantageous, and employed a similar formulation of the canopy snow cover fraction to incorporate the albedo influence of the new intercepted canopy snow storage.

$$f_{\text{cansnow}} = (W_{\text{snow}}/W^{\text{snow}}_{\text{max}})^{c_5} \tag{21}$$

We evaluated a spectrum of values for the c_5 exponent globally in standalone CLM 4.5 simulations forced with atmospheric data from *Qian et al.*, [2006]. Land model output was compared against the MODIS MCD43C3 (collection 5) 16-day visible black-sky albedo (VBSA) product, both evaluated from years 2001-2004. 0.05° resolution MODIS data defined with quality flag 2 or better were regridded to the 1.9° by 2.5° grid applied in our CLM simulations, using conservative area-overlap averaging of input pixels and with output defined where more than 1% of the grid cell area was covered with valid measurements. Monthly average albedo was calculated from weighted averages of the 16-day data, with weights determined by time overlap period. Data coverage varies with time of year due to insolation. e.g., North Hemisphere (NH) domains are limited to ~60° N in December. Differences in surface albedo translate into larger differences in the surface energy budget when and where there is greater insolation. To account for this we compare model and MODIS-derived surface net visible direct shortwave (NVDSW) radiation. The MODIS-derived quantity utilizes satellite VBSA and the same downwelling flux used in the CLM atmospheric forcing, as described in *Qian et al.*, [2006], ensuring that any radiation differences are caused only by albedo differences. This metric therefore functions essentially as an insolation-weighted average of visible albedo. We also evaluated visible direct albedo at local noon (VDALN), compared directly to MODIS visible black-sky albedo [*Schaaf et al.*, 2002]. The root-mean-square-error (RMSE) of MCD43 blue-sky albedo over Greenland compared to in-situ measurements was reported to be 0.067 during 2000-2012 [*Stroeve et al.*, 2013]. This quantity is not directly comparable to the data used in this paper because the study used a different quality flag, includes the influence of ice sheets and not vegetation, and blue-sky introduces more uncertainty by employing black-

sky and white-sky albedos in the calculation. Still, this provides a rough measure of the uncertainty of the observation data we employed.

We employed two error metrics for both NVDSW and VDALN to evaluate results from the contexts of both regionally-averaged quantities and also gridcell-by-gridcell performance. First, the RMSE of all gridcells in a region was calculated for each month with albedo value at longitude coordinate i and latitude coordinate j being α_{ij}^{model} and gridcell area being a_{ij}:

$$\text{Gridcell RMSE} = \sqrt{\sum_i^{lat}\sum_j^{lon}\left(\alpha_{ij}^{model} - \alpha_{ij}^{obs}\right)^2 a_{ij} / \sum_i^{lat}\sum_j^{lon} a_{ij}}. \quad (22)$$

This error, hence referred to as G-RMSE, was calculated for surface shortwave flux as well as albedo. These values are compared with a control run of unmodified CLM, presented as a percent change in Table 3-1. The cumulative gridcell error for all months in

	VDALN				NVDSW			
Trial	Δ R-RMSE	% Δ R-RMSE	Cum. Δ G-RMSE	% Cum. Δ G-RMSE	Δ R-RMSE	% Δ R-RMSE	Cum. Δ G-RMSE	% Cum. Δ G-RMSE
Base	-0.008	-14.0	-0.093	-9.2	0.038	1.9	-1.36	-3.7
Alb-Opt	-0.010	-17.6	-0.113	-11.2	-0.048	-2.5	-0.87	-2.4
fc1	-0.004	-7.0	-0.036	-3.6	0.167	8.6	-1.53	-4.2
fc3	-0.010	-17.3	-0.106	-10.5	-0.069	-3.6	-0.44	-1.2
fp1	-0.009	-15.5	-0.104	-10.3	0.014	0.7	-1.27	-3.5
fp2	-0.008	-14.9	-0.101	-9.9	0.023	1.2	-1.36	-3.7
sn1	-0.008	-14.0	-0.093	-9.2	0.038	2.0	-1.35	-3.7
sn3	-0.008	-14.0	-0.093	-9.2	0.037	1.9	-1.37	-3.8
ut1	-0.008	-14.0	-0.090	-8.9	0.046	2.4	-1.35	-3.7
ut3	-0.008	-14.0	-0.097	-9.6	0.027	1.4	-1.36	-3.7
uw1	-0.007	-11.6	-0.076	-7.5	0.059	3.1	-1.30	-3.6
uw3	-0.009	-15.8	-0.106	-10.5	0.016	0.8	-1.41	-3.9

Table 3-1: North Hemisphere error changes for albedo (VDALN) and surface shortwave

(NVDSW), in relation to unmodified CLM (Negative indicates improvement). From left to right is change in regional RMSE (Δ R-RMSE), percent change in regional RMSE (% Δ R-RMSE), Cumulative change in gridcell RMSE (Cum. Δ G-RMSE), and percent change in cumulative change in gridcell RMSE (% Cum. Δ G-RMSE).

a mean annual cycle was used for an annual metric (Table 3-1). Second, an annual RMSE was calculated for multiple regions for each month using regionally-averaged monthly mean values. For albedo, the regional RMSE (R-RMSE) using monthly regional-mean model albedo $\overline{\alpha_m^{model}}$ and MODIS value $\overline{\alpha_m^{obs}}$ is:

$$\text{Regional RMSE} = \sqrt{\sum_{\text{months}}(\overline{\alpha_m^{model}} - \overline{\alpha_m^{obs}})^2/12}. \quad (23)$$

These are also presented as a percent change from the control run values in Table 3-1. Regions evaluated are labeled in Figure 3-3 with their spatial domains. The top row plots

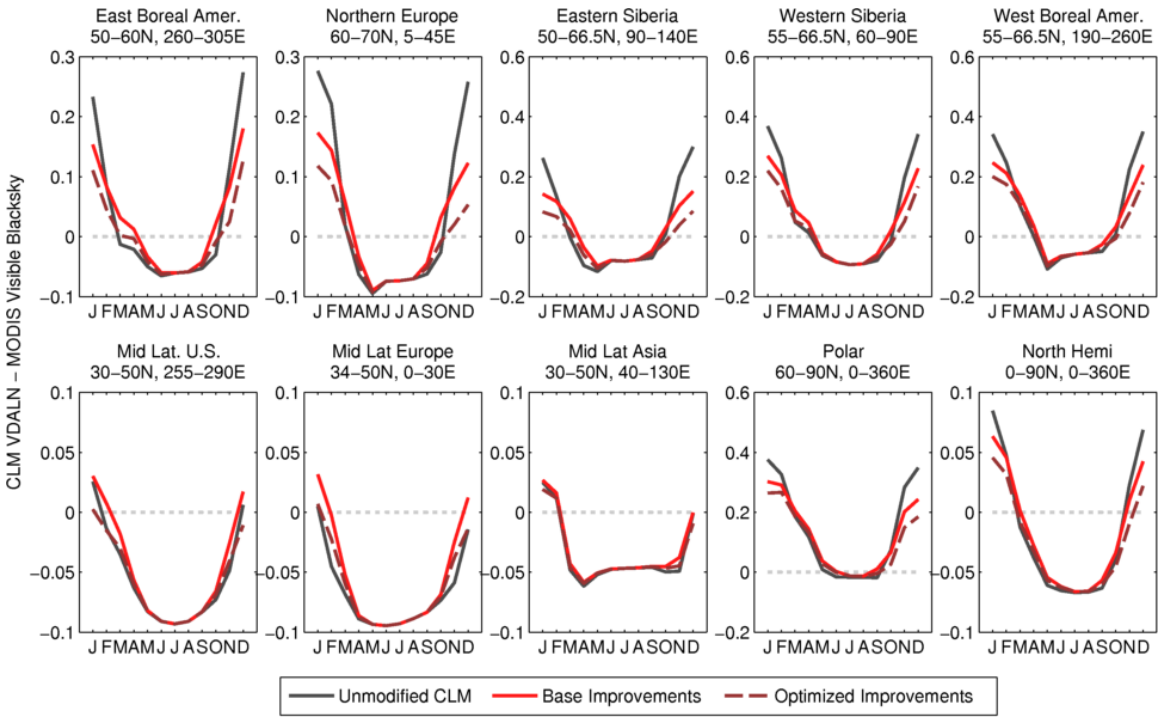

Figure 3-3: Land model direct visible albedo at local noon subtracted by MODIS visible black-sky albedo for selected boreal-forest dominated regions, lower-latitude U.S., high-latitude northern polar region, and Northern Hemisphere average.

boreal forest-containing regions, of particular interest to this study. From this analysis, a value of c_5=0.1 was ultimately selected for the base configuration. This selection reflects the realistic assumption that an initial snow deposition on bare vegetation will increase albedo significantly, while additional snowfall will not yield as much of a change.

3.3 Results

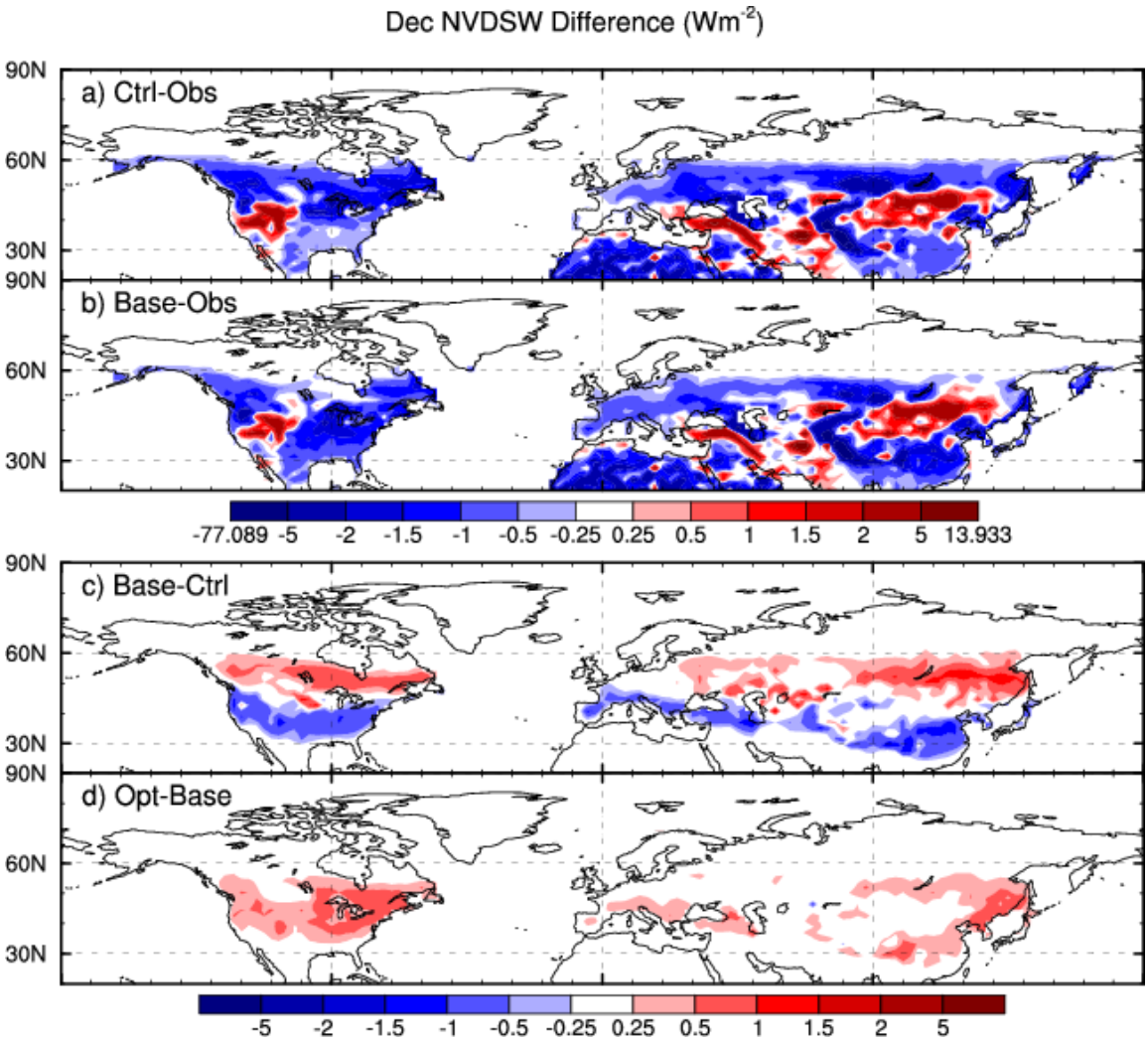

Figure 3-4: Difference in net visible direct shortwave at the surface in December, for a) Unmodified control run of CLM – MODIS-derived NVDSW, b) the base configuration of snow canopy vegetation modifications – MODIS-derived NVDSW, c) the albedo-optimized configuration – unmodified CLM, and d) Albedo-optimized configuration – the base configuration.

The newly-implemented treatment reduced global visible direct albedo compared to unmodified CLM, with particular improvement resulting from lowering mid-winter values (Figure 3-4), especially in regions containing large amounts of boreal forests ('base' simulation shown in Figure 3-3). This is a result of the tuning of intercepted snow

reflectance to satellite data, as well as the creation of unloading pathways allowing snow to leave canopy at temperatures below freezing [*Thackeray et al.*, 2014]. These improvements caused a winter seasonal (DJF) average R-RMSE improvement of 30% over the boreal zones. Mid latitude and polar zones also showed improvements, resulting in a 20% reduction in the R-RMSE of North Hemisphere land albedo in the winter season. Boreal zone albedo increases during March and April, slowing the springtime decline, which was known to occur too rapidly, by allowing the presence of snow to exist radiatively at temperatures above freezing [*Thackeray et al.*, 2014]. A harmful model feedback loop is eliminated, since canopy snow does not instantly disappear when vegetation temperatures increase above freezing, allowing for a sudden increase in insolation absorbed by the vegetation. Spring (MAM) seasonal average R-RMSE decreased 13% over the boreal zones when absolute G-RMSE peaks (Table 3-2), and 5% over the NH.

		Month												
Trial	Region	J	F	M	A	M	J	J	A	S	O	N	D	Y
Control	North Hemi.	0.15	0.13	0.10	0.09	0.09	0.05	0.03	0.03	0.04	0.07	0.10	0.14	1.01
	East Boreal Amer.	0.19	0.12	0.16	0.14	0.10	0.05	0.01	0.01	0.01	0.06	0.13	0.24	1.20
	Eastern Siberia	0.23	0.18	0.14	0.19	0.15	0.02	0.01	0.01	0.02	0.09	0.19	0.24	1.47
	Mid Lat Asia	0.16	0.17	0.12	0.07	0.03	0.03	0.03	0.03	0.03	0.02	0.05	0.12	0.85
	Mid Lat Europe	0.11	0.09	0.08	0.03	0.01	0.01	0.01	0.01	0.01	0.01	0.03	0.09	0.49
	Mid Lat. U.S.	0.09	0.08	0.10	0.04	0.01	0.01	0.01	0.01	0.01	0.01	0.04	0.09	0.52
	Northern Europe	0.18	0.19	0.15	0.17	0.12	0.04	0.01	0.01	0.01	0.05	0.14	0.19	1.26
	Polar	0.25	0.22	0.14	0.12	0.18	0.12	0.07	0.06	0.08	0.14	0.21	0.24	1.82
	West Boreal Amer.	0.28	0.23	0.16	0.13	0.17	0.05	0.02	0.02	0.02	0.09	0.21	0.28	1.68
	Western Siberia	0.31	0.24	0.15	0.13	0.06	0.01	0.00	0.00	0.01	0.08	0.17	0.26	1.43
Base	North Hemi.	0.12	0.12	0.10	0.08	0.08	0.05	0.04	0.04	0.04	0.07	0.08	0.10	0.92
	East Boreal Amer.	0.14	0.11	0.12	0.12	0.09	0.05	0.01	0.01	0.02	0.08	0.10	0.17	1.00
	Eastern Siberia	0.14	0.14	0.12	0.14	0.13	0.02	0.01	0.01	0.03	0.10	0.11	0.13	1.08
	Mid Lat Asia	0.15	0.16	0.11	0.06	0.03	0.03	0.03	0.03	0.03	0.02	0.05	0.11	0.83
	Mid Lat Europe	0.11	0.10	0.08	0.03	0.01	0.01	0.01	0.01	0.01	0.02	0.07	0.09	0.53
	Mid Lat. U.S.	0.09	0.08	0.09	0.04	0.01	0.01	0.01	0.01	0.01	0.02	0.06	0.09	0.53
	Northern Europe	0.10	0.15	0.12	0.15	0.12	0.04	0.01	0.01	0.03	0.08	0.09	0.09	0.99
	Polar	0.20	0.19	0.14	0.12	0.15	0.12	0.08	0.07	0.08	0.15	0.17	0.19	1.66
	West Boreal Amer.	0.21	0.20	0.15	0.11	0.15	0.05	0.02	0.02	0.04	0.11	0.16	0.20	1.44
	Western Siberia	0.23	0.20	0.13	0.12	0.05	0.01	0.00	0.00	0.02	0.09	0.10	0.16	1.13
Alb-Opt	North Hemi.	0.11	0.11	0.10	0.08	0.08	0.05	0.04	0.04	0.04	0.08	0.08	0.09	0.90
	East Boreal Amer.	0.13	0.12	0.14	0.13	0.09	0.05	0.01	0.01	0.02	0.06	0.08	0.14	0.98
	Eastern Siberia	0.12	0.14	0.13	0.16	0.14	0.02	0.01	0.01	0.02	0.09	0.09	0.12	1.04
	Mid Lat Asia	0.15	0.16	0.11	0.06	0.03	0.03	0.03	0.03	0.03	0.02	0.05	0.11	0.83
	Mid Lat Europe	0.09	0.09	0.07	0.03	0.01	0.01	0.01	0.01	0.01	0.01	0.05	0.07	0.46
	Mid Lat. U.S.	0.07	0.08	0.09	0.04	0.01	0.01	0.01	0.01	0.01	0.02	0.04	0.06	0.47
	Northern Europe	0.11	0.14	0.14	0.16	0.12	0.04	0.01	0.01	0.02	0.06	0.08	0.10	0.97
	Polar	0.19	0.17	0.14	0.12	0.16	0.12	0.08	0.07	0.08	0.17	0.17	0.20	1.66
	West Boreal Amer.	0.19	0.19	0.15	0.12	0.16	0.05	0.02	0.02	0.03	0.10	0.15	0.18	1.36
	Western Siberia	0.26	0.22	0.14	0.12	0.04	0.01	0.00	0.00	0.04	0.13	0.15	0.20	1.30

Table 3-2: Monthly gridcell RMSE (G-RMSE) for model visible direct albedo at local noon compared to MODIS VBSA. Cumulative of all months in column “Y”.

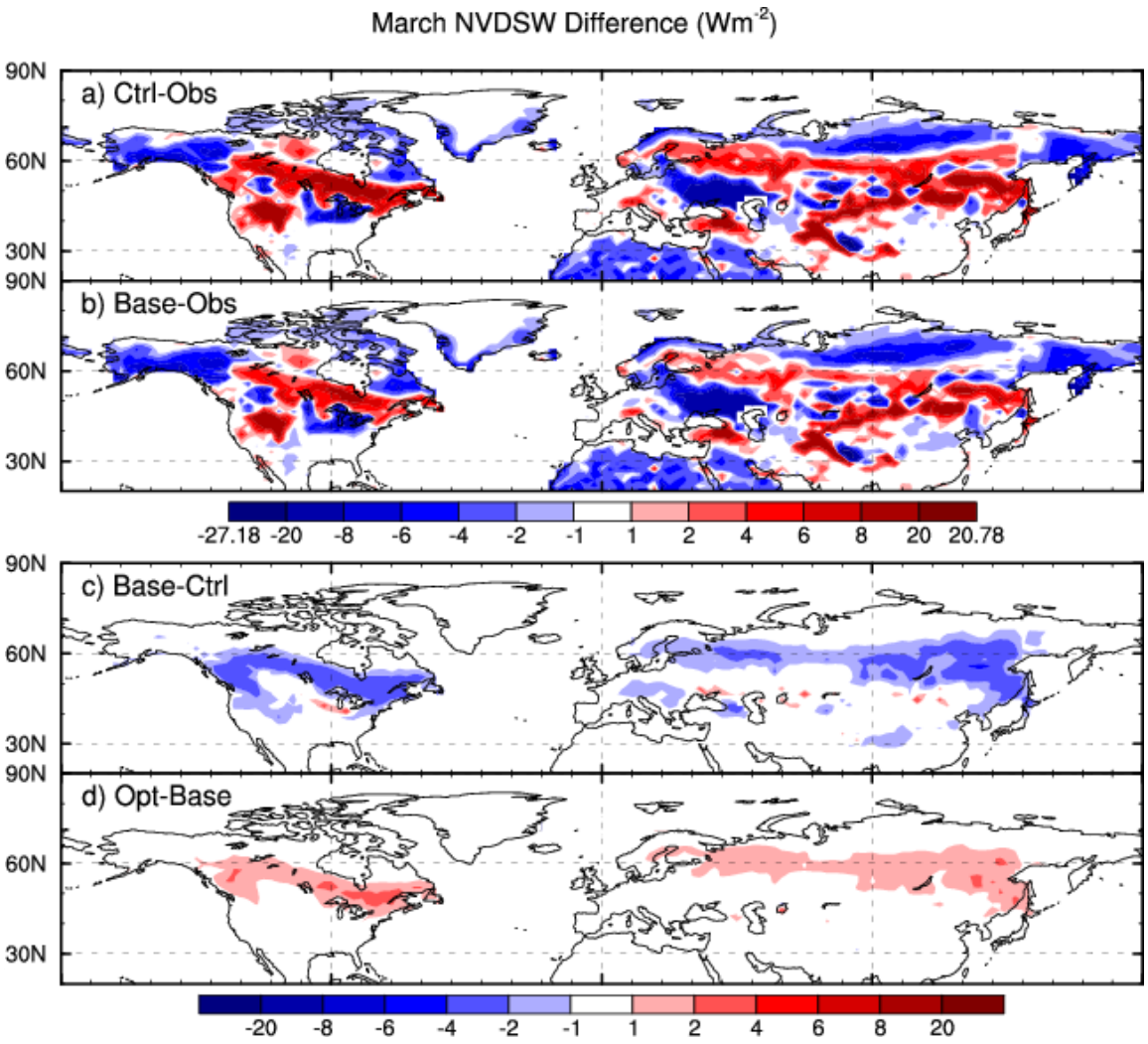

Figure 3-5: Difference in net SW at the surface in March, for a) Unmodified run of CLM – MODIS-derived NVDSW, b) the base configuration of snow canopy vegetation modifications – MODIS-derived NVDSW, c) the albedo-optimized configuration – unmodified CLM, and d) The albedo-optimized configuration – the base configuration.

The regionally average albedo improvements in the boreal forest regions are accompanied by declines in cumulative gridcell error, with bias reduction in winter and spring outweighing worsening bias in autumn (Table 3-2, Figure 3-5). The snow vegetation implementation worsens mid-latitude regions' cumulative G-RMSE, due to spatial heterogeneity of albedo biases. For example, March albedo is biased low for southeastern United States, while parts of the Western U.S. are biased high (Figure 3-6). The

modifications' general trend of lowering spring albedo assists the Western high biases, but harms the South-central and Eastern U.S. Mid-latitude biases are worsened in autumn despite regional averages showing improvement (Figure 3-3). The strong improvements made for boreal spring and winter outweigh detriments, giving the North Hemisphere a 9% reduction in cumulative G-RMSE over the annual cycle. Mean gridcell error increased for summer snow-affected regions in high northern latitudes that were already biased low.

Similar behavior is revealed in evaluation of the net direct shortwave statistics, but with insolation weighting spring changes more than winter in annual mean error statistics (Table 3-3). Spring seasonally average G-RMSE reduction is 15% over the boreal zones

		Month												
Trial	Region	J	F	M	A	M	J	J	A	S	O	N	D	Y
Control	North Hemi.	2.18	3.31	4.34	5.02	6.37	4.34	2.83	2.22	1.73	1.39	1.21	1.43	36.36
	East Boreal Amer.	1.35	2.43	6.56	8.82	7.90	3.89	0.59	0.62	0.47	1.02	0.91	1.10	35.65
	Eastern Siberia	1.43	3.06	5.42	10.58	10.65	1.31	0.46	0.49	0.56	1.20	1.13	1.17	37.45
	Mid Lat Asia	4.30	6.73	6.47	4.71	2.94	2.47	2.75	2.61	1.81	1.02	1.34	2.19	39.36
	Mid Lat Europe	1.05	1.85	2.90	1.56	0.84	0.94	0.95	0.78	0.58	0.45	0.42	0.61	12.92
	Mid Lat. U.S.	1.48	2.44	4.55	2.67	1.10	1.14	1.32	1.11	0.81	0.57	0.65	1.02	18.84
	Northern Europe	0.19	0.84	2.90	7.64	7.86	2.45	0.55	0.50	0.35	0.43	0.20	0.12	24.04
	Polar	0.35	1.38	2.86	5.92	12.75	8.93	4.42	2.31	1.32	0.98	0.39	0.19	41.80
	West Boreal Amer.	0.88	2.02	4.69	7.31	12.74	3.88	1.63	1.36	0.74	1.08	0.86	0.56	37.76
	Western Siberia	1.01	2.05	4.00	6.84	4.07	0.71	0.25	0.24	0.23	0.78	0.59	0.68	21.46
Base	North Hemi.	2.08	3.17	4.03	4.56	5.61	4.26	3.07	2.33	1.78	1.47	1.22	1.41	34.99
	East Boreal Amer.	0.95	2.15	5.02	7.25	6.66	3.45	0.65	0.70	0.93	1.46	0.86	0.71	30.78
	Eastern Siberia	1.10	2.49	4.31	8.37	9.12	1.06	0.47	0.57	0.96	1.50	0.87	0.78	31.60
	Mid Lat Asia	4.08	6.51	6.25	4.58	2.97	2.50	2.77	2.63	1.89	1.11	1.36	2.21	38.86
	Mid Lat Europe	1.06	1.86	2.85	1.44	0.84	0.93	0.95	0.78	0.58	0.54	0.69	0.62	13.14
	Mid Lat. U.S.	1.53	2.31	3.97	2.85	1.20	1.15	1.32	1.11	0.84	0.81	1.03	1.18	19.28
	Northern Europe	0.11	0.64	2.22	6.51	7.41	2.43	0.56	0.52	0.60	0.65	0.16	0.06	21.86
	Polar	0.28	1.21	2.93	5.70	10.87	8.74	5.28	2.81	1.49	1.06	0.30	0.16	40.84
	West Boreal Amer.	0.62	1.90	4.40	6.32	11.13	3.49	1.63	1.41	1.17	1.33	0.65	0.36	34.42
	Western Siberia	0.72	1.79	3.46	6.19	3.35	0.58	0.25	0.25	0.62	0.98	0.41	0.51	19.12
Alb-Opt	North Hemi.	2.04	3.20	4.15	4.76	5.91	4.30	3.06	2.31	1.76	1.44	1.18	1.37	35.48
	East Boreal Amer.	0.92	2.65	6.02	8.08	7.24	3.61	0.62	0.66	0.73	1.10	0.65	0.58	32.86
	Eastern Siberia	1.07	2.73	4.89	9.41	9.75	1.14	0.47	0.53	0.71	1.25	0.73	0.71	33.40
	Mid Lat Asia	4.05	6.54	6.32	4.62	2.96	2.49	2.77	2.62	1.86	1.06	1.36	2.18	38.82
	Mid Lat Europe	0.90	1.68	2.81	1.48	0.84	0.93	0.95	0.78	0.58	0.50	0.54	0.51	12.50
	Mid Lat. U.S.	1.28	2.41	4.12	2.71	1.17	1.14	1.32	1.11	0.83	0.70	0.78	0.86	18.43
	Northern Europe	0.10	0.62	2.77	7.05	7.60	2.43	0.56	0.51	0.48	0.44	0.15	0.07	22.79
	Polar	0.26	1.09	2.83	5.76	11.61	8.84	5.26	2.76	1.41	1.18	0.30	0.16	41.47
	West Boreal Amer.	0.52	1.80	4.50	6.79	11.84	3.58	1.63	1.39	0.94	1.18	0.51	0.29	34.98
	Western Siberia	0.61	1.58	3.81	6.45	3.79	0.63	0.25	0.25	0.43	0.80	0.29	0.45	19.33

Table 3-3: Monthly gridcell RMSE for model net visible direct shortwave (NVDSW) compared to MODIS-derived NVDSW. Cumulative R-RMSE of all months in column "Y".

and 9% over north hemisphere land. Winter average G-RMSE is 27% and 3% respectively over the same regions. The cumulative G-RMSE averaged over all the boreal zones

decreases 12% due to the delay in albedo decline, while R-RMSE NVDSW diminished 30% over the same areas. Rising net shortwave radiation overall detrimentally affects mid-latitude winter and fall, although improvements were made in some mid-latitude areas biased high during spring. Despite a cumulative annual NH G-RMSE reduction of 4%, the NH R-RMSE increased by 2%. That is to say, the snow vegetation implementations improve the gridcell-by-gridcell error, but the NH average shortwave is worsened because of pre-existing biases in regions less affected by snow. The smaller vernal albedo universally benefits the boreal zones, but over the whole hemisphere alters the season's NVDSW so strongly that it switches from a positive bias to a negative one (Figure 3-8).

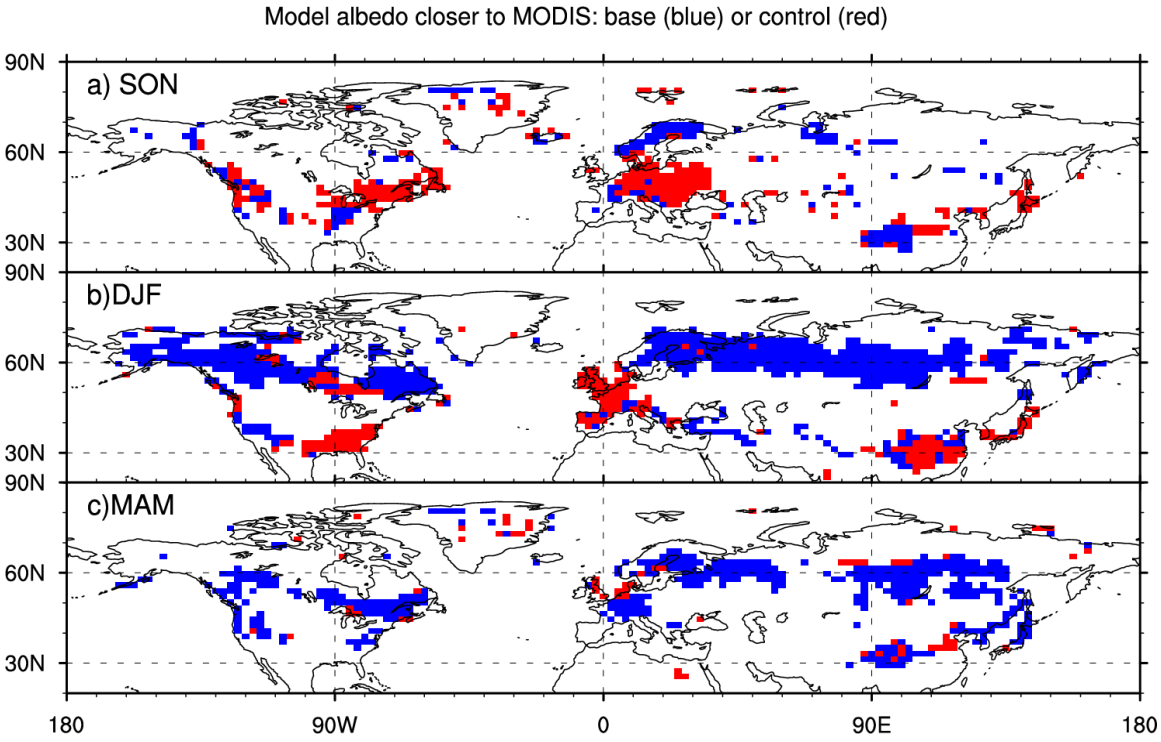

Figure 3-7: Closer fitting model between base configuration and unmodified CLM control, comparing model VDALN with MODIS VBSA at 95% confidence level.

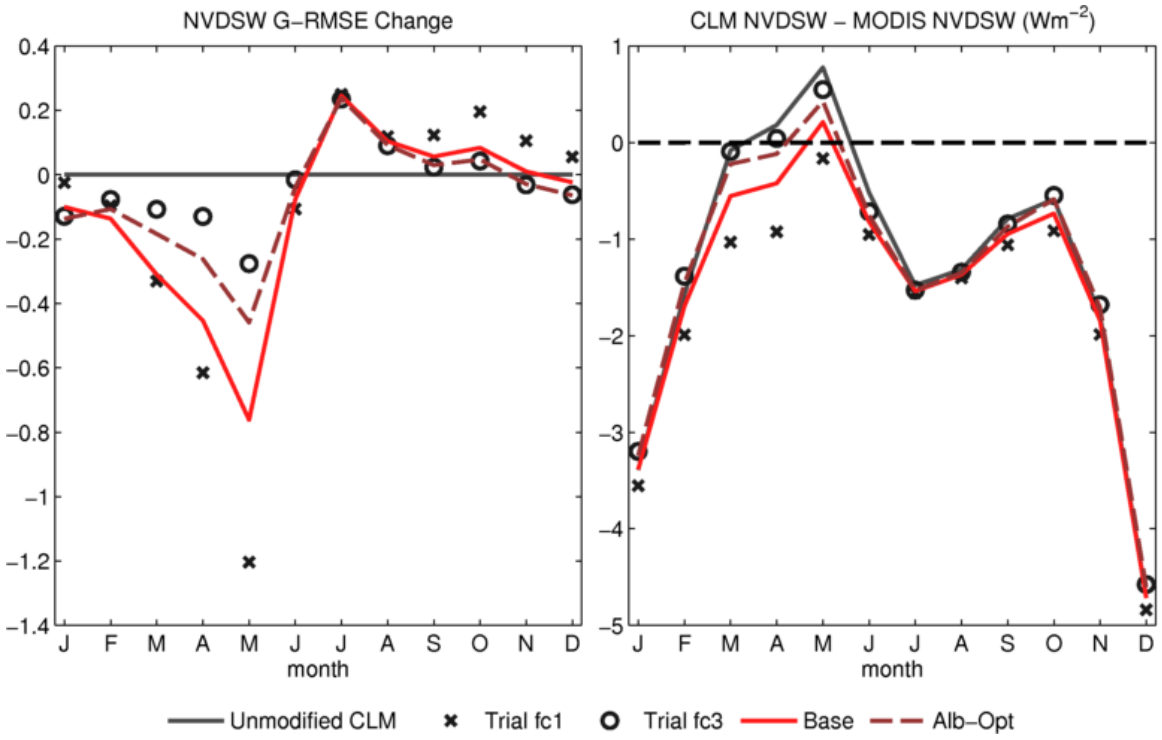

Figure 3-8: G-RMSE change for model net visible direct shortwave compared to control over North Hemisphere land (left). Model error for each compared with MODIS-derived NVDSW was averaged monthly, and compared to unmodified CLM. (Right) Monthly regional NVDSW over the same domain.

3.4 Parameter Exploration

The impacts of individual parameters in the new canopy snow implementation were explored via multiple standalone CLM 4.5 simulations. In the base configuration, exponential weighting of intercepted snow in $f_{cansnow}$ was tuned to MODIS albedo. Some further variation of this value was involved in the sensitivity study. Additionally, variations of the maximum snow storage limit, interception efficiency, and unloading fluxes were also explored with the present day global simulations. A summary of the trials appears in Table 3-4.

Parameter varied	Trial Prefix	Trial #		
		1	2	3
c_5 in Eq. (21), unitless	fc	0.05	**0.1**	0.2
c_4 in Eq. (17), kg m^{-2}	sn	4	**6**	8
c_1 in Eq. (3), unitless	fp	0.25	0.5	**1**
c_2 in Eq. (14), m	uw	$4.67x10^4$	**$9.35x10^4$**	$1.87x10^5$
c_3 in Eq. (15), K s	ut	$7.8x10^4$	**$1.56x10^5$**	$3.12x10^5$

Table 3-4: Selected parameter values explored in standalone CLM sensitivity study (base values are bold).

3.4.1 Intercepted snow cover fraction.

As would be expected, higher values of the $f_{cansnow}$ exponent decreased albedo, while lowers values increased it. This turns out to be the most sensitive parameter studied. The base configuration value of c_5=0.1 was adjusted between c_5=0.05 (trial fc1) and c_5=0.2 (trial fc2). Neither trial significantly improves the net SW bias, for different reasons. Lowering c_5 for fc1 brightened albedo that was already too reflective in almost all model regions in winter (Figure 3-9). The brightening albedo benefited spring for boreal regions

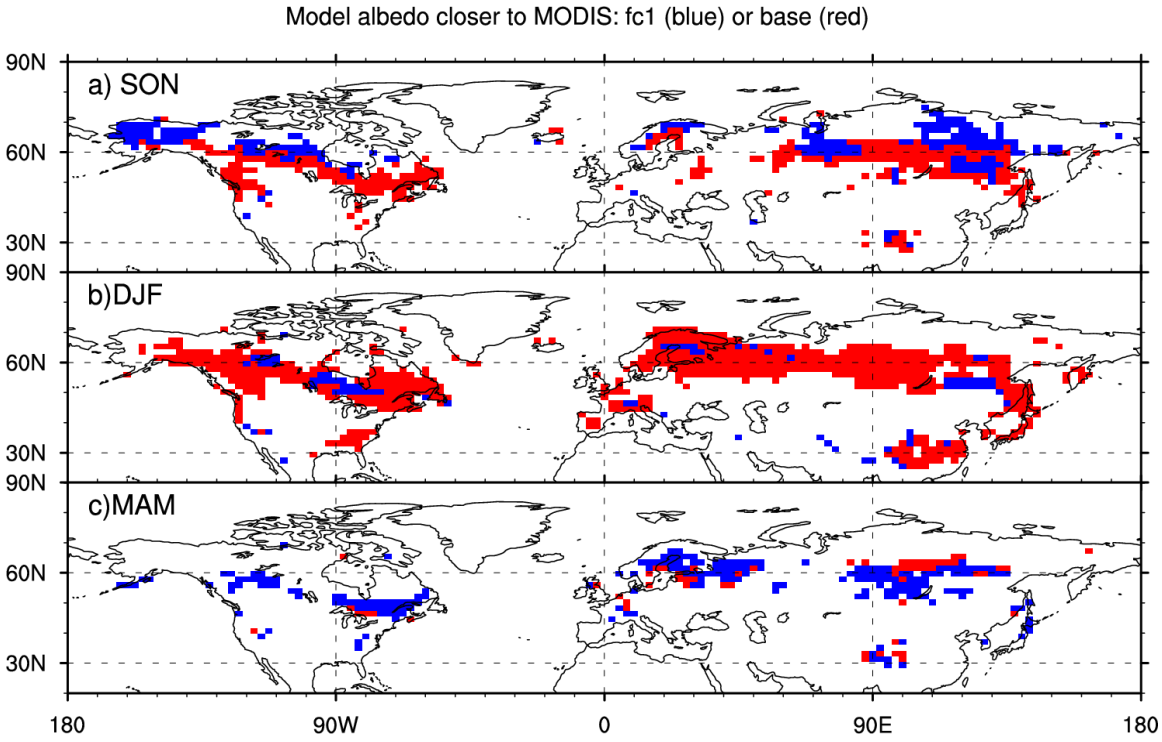

Figure 3-9: Closer fitting model between trial fc1 and base configuration, comparing model VDALN with MODIS VBSA at 95% confidence level.

but hindered small areas in high polar regions and some lower latitudes. The change in NH R-RMSE was +8%, and the cumulative G-ΔRMSE was +0.5 greater than the base configuration. Albedo for the fc1 trial also saw increase in annual grid cell and regional mean errors, especially for autumn.

Increasing c_5 in trial fc3 resulted in a further 1% reduction in cumulative G-RMSE for albedo (Table 3-1). Comparing with control, fc3 further lowered NH G-RMSE by an average of 6% in winter months (DJF), benefiting largely from the further reduction in high boreal region bias compared to MODIS (Figure 3-10). This was compensated by a 5% increasing error compared with base configuration in spring months (MAM), stemming

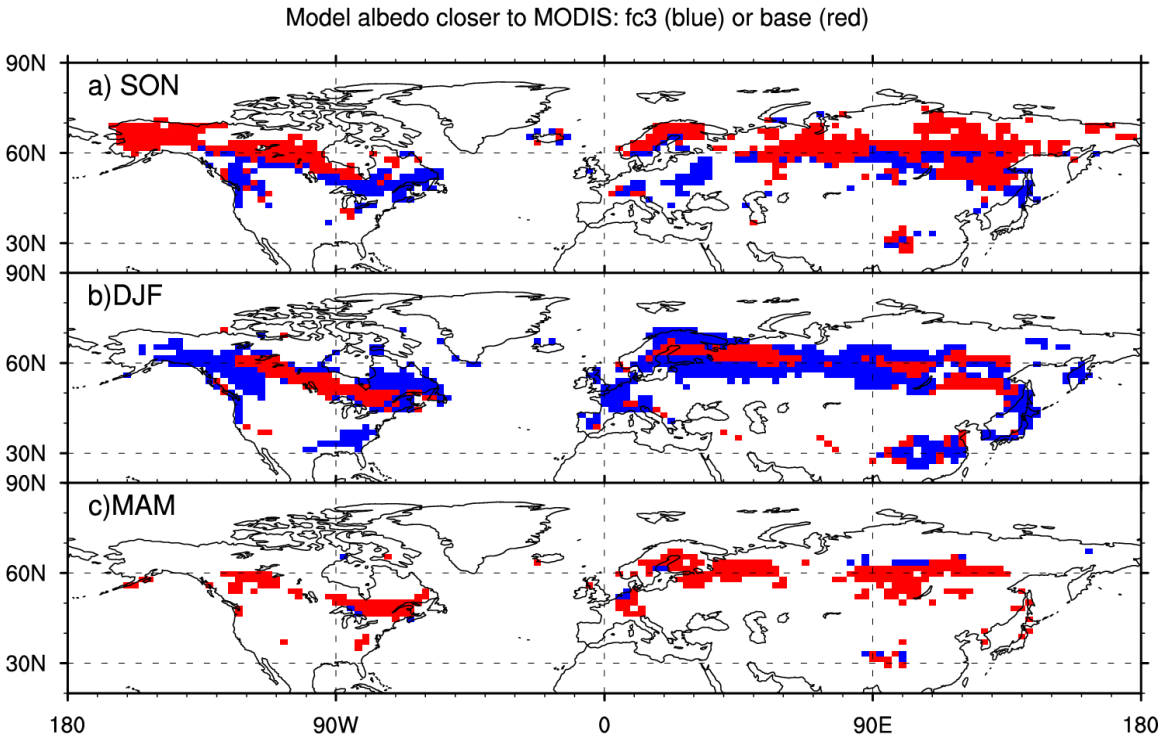

Figure 3-10: Closer fitting model between trial fc3 and base configuration, comparing model VDALN with MODIS VBSA at 95% confidence level.

mostly from removal of the improved albedo decline timing in boreal zones. Improvements in fall led to the 3% overall G-RMSE reduction.

Comparing NVDSW biases in the fc3 trial, average March gridcell RMSE in the boreal zones increased 16% over the base, contributing to a 6% increase in North Hemisphere G-RMSE. Better alignment with autumn albedo increase greatly reduced gridcell error compared to base, as much as 50% in Western Siberia, and 40% in East boreal America, resulting in a 3% NH G-RMSE reduction. With a 1% improvement in winter, this netted a 2.5% increase in NH G-RMSE over base, but still a 1% reduction over control. In terms of cumulative gridcell error, the fc3 trial universally harmed boreal zones but improved some lower-latitude regions like the mid-latitude US and Europe. The same behavior is seen in the regional means. The NH R-RMSE is reduced compared to the

control, resulting from boreal and polar zones with higher cumulative G-RMSE and lower latitudes with lower G-RMSE. Trial fc3 reduces NH R-RMSE by 4% compared to the control run, or 6% compared to the base configuration. This is largely due to albedo increases in spring closing the NH regionally-averaged radiation gap. However, the majority of these increases come from boreal zones where spring albedo in the base configuration was already too high.

Additional trials between $c_5 = 0.08$ and $c_5 = 0.2$ were conducted, attempting to compromise with a global reduction in monthly net shortwave biases, as well as net reductions in gridcell errors. For a configuration optimizing albedo error reduction, $c_5$was selected to be 0.15.

3.4.2 Maximum storage interception

$W_{\underset{max}{snow}}$ was tuned to the in-situ canopy interception measurements along with unloading fluxes to provide appropriate canopy snow retention. Similarly, we varied c_4 in $W_{\underset{max}{snow}}$ in the global present-day simulations from 4 kg m^{-2} (trial sn1) to 8 kg m^{-2} (trial sn3) times the combined leaf and stem area indices. As expected, lowering $W_{\underset{max}{snow}}$ to 4x decreases albedo, but only slightly, and there was a 0% change in both the regional RMSEs and the cumulative gridcell RMSEs compared to base. The conclusion is similar to that for raising $W_{\underset{max}{snow}}$ to 8x, with a 0% change in errors.

3.4.3 Interception efficiency

In unmodified CLM, the interception in a time step is $\Delta W^{intr} = 0.25(q_{rain} + q_{snow})(1 - e^{-0.5(LAI+SAI)}) \cdot \Delta t$. The newly implemented snow canopy storage accepts snowfall at a rate of $\Delta W_{snow}^{intr} = (1.0 \cdot q_{snow})(1 - e^{-0.5(LAI+SAI)})$, while liquid interception rate remains unchanged. We selected an efficiency coefficient of 1.0 to allow for the large interception of snow on a leaf. In our study, we assessed the impacts of this change through trials lowering the interception efficiency c_1 in $\Delta W_{snow}^{intr} = (c_1 \cdot q_{snow})(1 - e^{-0.5(LAI+SAI)})$. Here we show the effect of $c_1 = 0.25$ (trial fp1) and an intermediate value of $c_1 = 0.5$ (trial fp2) compared to $c_1 = 1.0$ in the base configuration.

Trial fp1 did not significantly alter albedo in autumn and spring compared to the base configuration, but did cause some significant differences in winter (Figure 3-11). No

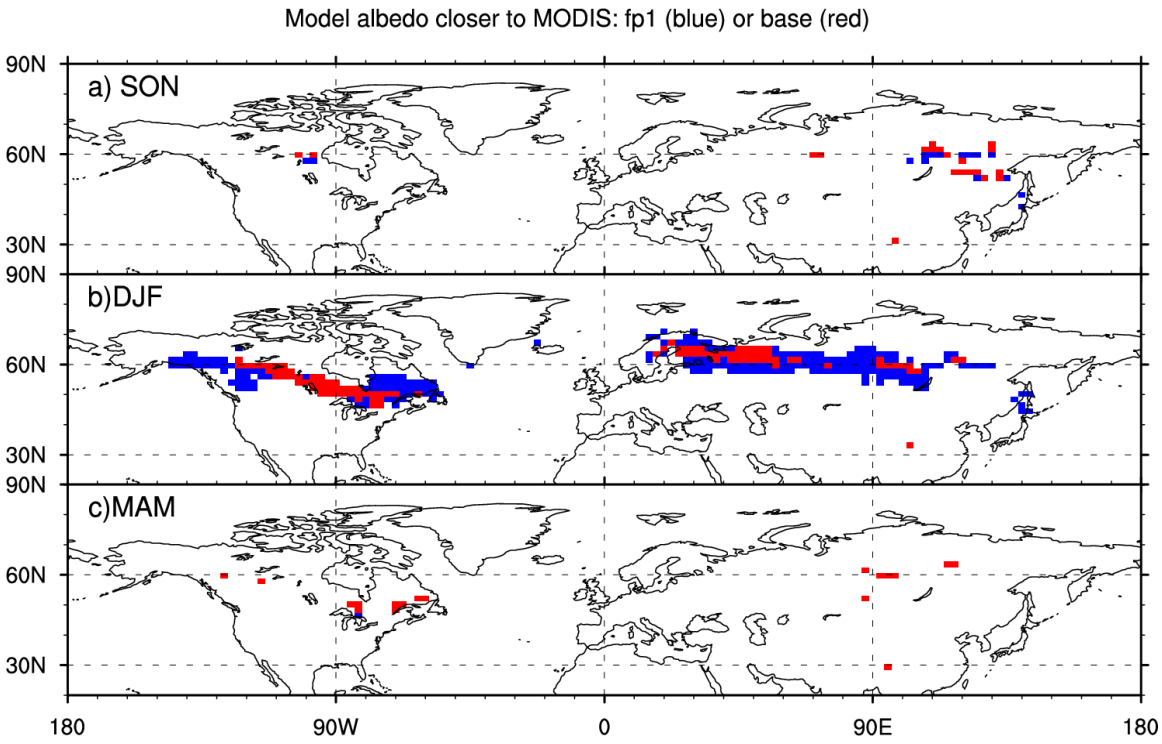

Figure 3-11: Closer fitting model between trial fp1 and base configuration, comparing model VDALN with MODIS VBSA at 95% confidence level.

studied regions' albedo changed by more than 0.02 compared to base. However, due to the spatial distribution of positive and negative biases, neither selection stood out as better in NH regional RMSE reduction. NH cumulative error reduction was 1% due to improvements in boreal winter. NVDSW cumulative gridcell RMSE increased in relation to the base configuration, but changes were below statistical significance for a p-value of 0.05. The intermediate trial fp2 follows the same pattern of fp1, but with an even smaller proportion of significant winter changes compared to the base configuration.

3.4.4 Unloading Fluxes

In global evaluation runs, unloading rates were halved and doubled compared to the base configuration. In trial ut1, we halved the temperature unloading constant in Eq. (15). This showed small but statistically irrelevant changes in cumulative RMSE. Doubling

the temperature unloading (trial ut3) had a small improvement in annual North hemisphere error reduction due to lowering mid-winter albedo. NVDSW NH regional RMSE improved <1% over base. T-tests showed that few gridcell changes were significant at a p-value of 0.05. Increasing of unloading strength quickened spring albedo decline, benefiting some lower latitude areas, but diminishing the benefits of boreal-forest containing regions.

The strength of the wind unloading had larger impact. Halving the wind unloading strength c_2 in trial uw1 caused 2.4% and 1.1% increases in NH R-RMSE compared to the base configuration for albedo and net shortwave, respectively. The G-RMSE in winter and fall increased for all studied regions, while the remainder of the year saw relatively little error change. Conversely, decreasing albedo caused winter and autumn error reduction in all regions when wind unloading was doubled in trial uw3. For North Hemisphere land, this led to a 2% R-RMSE improvement in albedo, a 1% cumulative albedo G-RMSE reduction, and a 1% reduction in shortwave R-RMSE, despite small increases in spring error. While temperature unloading changes did not appear beneficial, the wind unloading constant $c_2$was doubled in the albedo-optimized case, matching the value suggested by *Roesch et al.*, [2001].

3.4.5 Albedo-Optimized Configuration.

We pursued an "optimized" configuration that would improve albedo gridcell error compared to MODIS, independent of insolation weighting. Decreasing the weighting of snow storage in the canopy cover fraction with $c_5 = 0.15$ and increasing the wind

unloading flux by doubling c_2 were the adjustments made between the base configuration and the albedo-optimized configuration.

The optimized configuration reduced albedo error, both in cumulative NH gridcell error, and in R-RMSE. A 6% reduction in winter (DJF) albedo G-RMSE, relative to the base configuration, led the improvement, with a further 2% reduction in fall months (SON). Boreal winter gridcell error was reduced 33% compared to control, with 28% and 25% reductions in mid-latitude U.S. and Europe, respectively, through darkening canopy. However, spring months (MAM) gained an average 3% gridcell RMSE relative to the base state due to declining albedo. Despite this, all studied regions except Northern Europe still experience a springtime reduction in error due to the snow hydrology implementation compared to control. Total NH G-RMSE was reduced 6% over spring and 23% over winter against unmodified CLM.

Insolation weighting highlights the worse spring performance in the NVDSW, with 8% G-RMSE in boreal regions' spring than the base configuration compared to unmodified CLM. Despite a 2% improvement in fall bias and 1% improvement in winter, the cumulative NH annual gridcell error was 1% greater than the base configuration with respect to control. Overall, the albedo-optimized configuration reduces North Hemisphere shortwave cumulative grid cell bias compared to the unchanged model. The annual cumulative RMSE was reduced 2.4%. Boreal zone winter bias was reduced 31% while spring bias was reduced another 7%. The R-RMSE of net shortwave was reduced 2.5% compared to control.

3.5 Summary & Conclusions

We incorporated an integrated hydrology-radiation scheme into CLM's vegetation treatment. Intercepted snow storage is now a prognostic variable, allowing accumulated canopy snow mass to be explicitly represented in the radiation scheme. Canopy snow interception and unloading variables were created and compared to 30-minute resolution interception measurements from the Umpqua Forest, with good agreement. Valid ranges of the parameters were explored with global offline land model simulations. MODIS MCD43C3 albedo data were used to evaluate the error reduction of multiple configurations in a variable sensitivity study.

In the base configuration, the RMSE for net visible direct shortwave flux in the boreal zone decreased 27% in winter, and 13% in spring. Despite an increase in autumn error, the annual cumulative gridcell RMSE was reduced 12% over the region. Cumulative gridcell direct visible albedo RMSE was reduced 20% over the same area. Most of the improvement was through decreased mid-winter albedo via canopy intercepted snow fraction tuning and the availability of freezing-temperature unloading fluxes, especially in boreal forest regions. Vernal improvement resulted from the delaying of spring darkening. Over the North Hemisphere, cumulative gridcell error was reduced 4% for shortwave flux and 9% for albedo. An albedo-optimized configuration reduced North Hemisphere cumulative albedo error by 11% relative to the unmodified model.

Further refinement can be made to these relatively simple additions to CLM. In particular, parameter adjustments that are specific to plant functional type would be expected to yield further improvements necessary for global employment. The in-situ canopy snow vegetation measurements employed were for needleleaf evergreens in a

warm, moist winter environment, and thus wouldn't be expected to be completely representative of boreal forests. Vegetation-specific interception and unloading parameters from multiple observational sources would allow for region-specific bias improvement.

Chapter 4

Simulated Climate Change under Future Forcing Scenarios with Improved Canopy Snow Representation

4.1 Introduction

Terrestrial snow cover area is reduced with rising temperatures, thereby increasing the solar energy absorbed by the land surface. This snow albedo feedback (SAF) has strong influences from vegetation [*Essery*, 2013; *Qu and Hall*, 2014]. Multiple scattering events lower albedo increasingly with lower zenith angles, especially for vertical canopy structure [*Henderson-Sellers and Wilson*, 1983]. Exposed, unburied vegetation dampens the SAF by masking the brightness of surface snow. Considering not just shortwave influences but total radiation effects, northern latitude forests in particular have been shown to increase both winter and summer surface temperatures where they are present [*Bonan et al.*, 1992], and to cause earlier snowmelt [*Niu and Yang*, 2004].

Here we consider the effects of employing snow vegetation canopy (SnowVegCan) modifications discussed in Chapter 3 in coupled atmosphere-ocean-land climate models. These modifications only impact snow-affected regions, and can alter modeled climate in several ways beyond SAF. Increased vegetative snow interception reduces snow depth and increases canopy sublimation. This as well as alterations to snowy vegetation albedo translate to a redistribution of intra-canopy and sub-canopy energy budget. As an example, midwinter boreal aboreal albedo is lowered by SnowVegCan (Chapter 3), thus also

increasing canopy sublimation, as well as heat transferred to ground. Changes in snow depth due to albedo changes have been noted to affect sub-canopy turbulent fluxes [*Niu and Yang*, 2004; *Chen et al.*, 2014]. One aspect is not considered; SnowVegCan does not directly alter intra-canopy roughness length. The response of vegetation cover to increased CO_2 concentrations is not considered here, though such changes modulate the effect of snow on climate, especially in arctic and sub-arctic regions [*Bergengren et al.*, 2001; *Bonfils et al.*, 2012].

4.2 Methods

The SnowVegCan modifications to CLM4.5 as discussed in Chapter 3 were implemented into CLM4.0 for the purposes of conducting coupled simulations. (CLM version 4.5 has not yet been coupled into an operational CESM framework with an active ocean component). The Community Earth System Model version 1.2.0 (CESM1.2) was operated in a pre-industrial configuration with CLM 4.0, the Community Atmosphere Model version 5 (CAM5), a slab ocean model, and a prognostic sea ice model (component set alias "E1850C5"). This was run with and without SnowVegCan, for two forcing scenarios. The first pair were with a prescribed CO_2 concentration of 280 parts per million (ppm), a roughly pre-industrial level [*Etheridge et al.*, 1996]. The second pair had a doubled CO_2 concentration of 560 ppm, beyond present-day levels. The simulations were allowed to equilibrate over 30 years, after which no transient changes were observed in surface temperature, top-of-atmosphere radiation balance, precipitation rate, or surface runoff rate. 15 years of post-equilibrated output was considered steady-state climatology and compared.

4.3 Analysis

We consider the evolution of global climate with and without the SnowVegCan employed, using changes in climate states described in Eq. (24) and Eq. (25). "Control" denotes the unmodified CESM1.2 simulations, "SnowVeg" the SnowVegCan-implemented simulations, and the subscripts indicate the prescribed CO_2 concentration in ppm. We also evaluate the difference in climate responses, "ΔEvolution" (Eq. 26)

$$\Delta\text{Control} = \text{Control}_{560} - \text{Control}_{280} \tag{24}$$

$$\Delta\text{SnowVeg} = \text{SnowVeg}_{560} - \text{SnowVeg}_{280} \tag{25}$$

$$\Delta\text{Evolution} = \Delta\text{SnowVeg} - \Delta\text{Control} \tag{26}$$

The CO_2 concentration doubling most strongly affects polar regions through sea ice loss, as seen in the unmodified CESM control runs (Figure 4-1, left). Strong albedo changes there are shown on the left side in Figure 4-2. Global mean surface temperature response to the forcing in the control simulations is 3.8 K (Table 4-1), near the peak of GCM ensemble responses to a CO2 doubling forcing [*Roe and Baker*, 2007]. Using model annual mean net Top-of-Model energy flux, this places the simulated climate sensitivity at λ = 0.46 K W^{-1} m^2 with and without SnowVegCan. North Hemisphere land surface warming was 5.0 K, corresponding with a 0.018 decrease in surface albedo under all-sky conditions. Winter (DJF) boreal changes were the largest of any season-hemisphere combination, with a 0.032 reduction in surface albedo and 5.7 K increase in surface temperature.

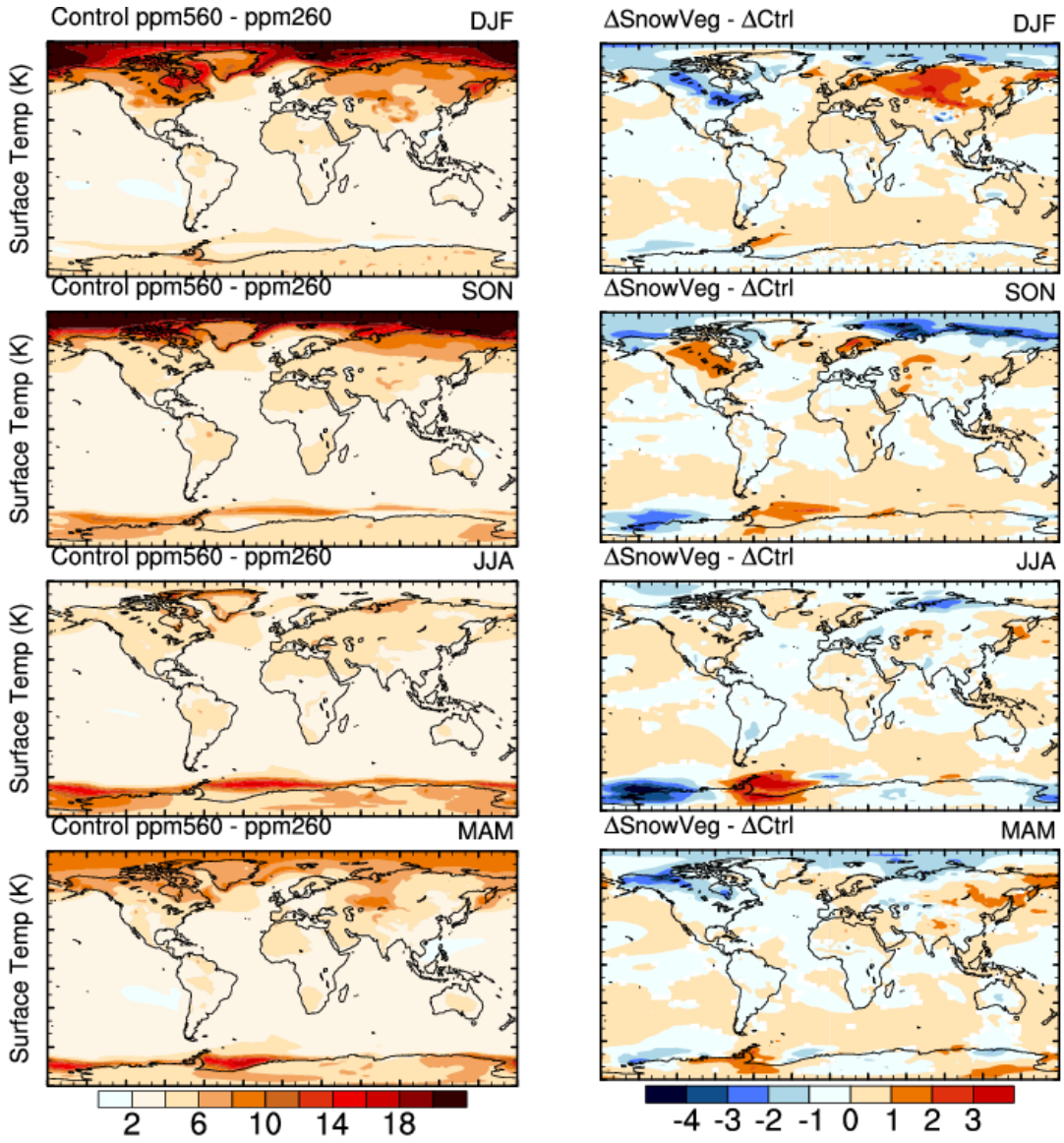

Figure 4-1: On the left, seasonally averaged evolution in surface temperature for the control, unmodified simulations. On the right, change in the surface temperature evolution between SnowVegCan implementations and the control simulations.

As a measure of SAF, global annual $\Delta\bar{\alpha}/\Delta\bar{T}$ is -0.37 %/K, with North Hemispheric land $\Delta\bar{\alpha}/\Delta\bar{T}$ equal to -0.36 %/K. Boreal terrestrial winter $\Delta\bar{\alpha}/\Delta\bar{T}$ was the maximum at -0.56 %/K, while summer was -0.14 %/K. The Extratropical NH (0-45° N) land SAF was -0.68 %/K, -0.83 %/K, -0.28 %/K, -0.59 %/K and -0.57 %/K for winter, spring, summer and fall respectively. Similarly-computed CMIP5 ensemble mean feedbacks are 0.7 %/K, 0.9

		Land ΔControl					Land ΔEvolution				
Variable	Domain	DJF	MAM	JJA	SON	ANN	DJF	MAM	JJA	SON	ANN
Albedo (%)	Global	-2.2	-1.6	-0.49	-1.2	-1.3	-0.028	0.022	0.009	0.095	7E-04
	North Hemi.	-3.2	-2.3	-0.62	-1.8	-1.8	-0.042	0.048	0.03	0.13	0.011
	South Hemi.	-0.21	-0.13	-0.12	-0.051	-0.14	-3E-04	-0.041	-0.049	0.015	-0.028
Downwelling Surf. SW (W m-2)	Global	-2.9	-1.8	1.2	-1.2	-1.2	-0.19	-0.79	-0.52	-0.013	-0.38
	North Hemi.	-2.7	-3.5	1.1	-2.6	-1.9	-0.39	0.19	-0.51	-0.26	-0.24
	South Hemi.	-3.3	1.7	1.6	1.6	0.4	0.22	-2.8	-0.54	0.5	-0.66
FSR (W m-2)	Global	-3.3	-4.1	-1.3	-1.6	-2.6	-0.038	-0.11	-0.09	-0.055	-0.074
	North Hemi.	-3.3	-6	-2	-1.9	-3.3	-0.082	0.09	-0.085	-0.11	-0.047
	South Hemi.	-3.1	-0.16	0.11	-0.91	-1	0.052	-0.53	-0.1	0.066	-0.13
SABV (W m-2)	Global	-0.087	0.75	1.8	0.34	0.71	0.09	-0.37	-0.1	0.085	-0.076
	North Hemi.	-0.42	0.4	2.2	-0.55	0.4	0.054	0.039	0.044	0.068	0.051
	South Hemi.	0.6	1.5	1.2	2.2	1.3	0.17	-1.2	-0.4	0.12	-0.34
Snow Frac. (%)	Global	-5	-4.4	-0.97	-3.9	-3.6	-0.27	0.054	0.048	-0.13	-0.074
	North Hemi.	-7.4	-6.5	-1.4	-5.8	-5.2	-0.38	0.088	0.11	-0.19	-0.096
	South Hemi.	-0.28	-0.25	-0.13	-0.12	-0.19	-0.023	-0.015	-0.069	-0.007	-0.029
Snowcover Days	Global	-0.52	-0.57	-0.37	-0.7	-0.54	-0.023	0.008	0.016	-0.006	0.006
	North Hemi.	-0.97	-1.1	-0.72	-1.4	-1	-0.044	0.018	0.037	-0.011	0.014
	South Hemi.	-0.068	-0.057	-0.026	-0.028	-0.045	-0.002	-0.003	-0.006	-0.001	-0.002
Surface Temp. (K)	Global	5.1	4.5	4.4	4.8	4.7	0.14	-0.08	-0.12	0.05	-0.004
	North Hemi.	5.7	4.6	4.4	5.1	5	0.24	-0.081	-0.066	0.045	0.033
	South Hemi.	3.9	4.2	4.4	4.3	4.2	-0.068	-0.078	-0.24	0.062	-0.081
Veg. Temp. (K)	Global	5.1	4.4	4.5	4.8	4.7	0.13	-0.079	-0.13	0.039	-0.011
	North Hemi.	5.6	4.6	4.4	5	4.9	0.22	-0.073	-0.077	0.027	0.025
	South Hemi.	3.9	4.2	4.5	4.4	4.2	-0.063	-0.091	-0.25	0.061	-0.085

		ΔControl					ΔEvolution				
Variable	Domain	DJF	MAM	JJA	SON	ANN	DJF	MAM	JJA	SON	ANN
Albedo (%)	Global	-1.3	-1.3	-1.4	-1.4	-1.4	0.025	0.027	0.084	0.066	0.05
	North Hemi.	-1.8	-1.7	-1.7	-1.3	-1.6	0.028	0.025	0.17	0.17	0.099
	South Hemi.	-0.86	-0.85	-1.1	-1.5	-1.1	0.022	0.029	-0.006	-0.038	0.002
Net TOM SW (W m-2)	Global	3.1	3.9	5.1	4.1	4.1	0.43	0.062	-0.28	0.056	0.067
	North Hemi.	2.3	5.3	7.8	2.9	4.6	0.45	0.31	-0.39	-0.27	0.023
	South Hemi.	3.9	2.5	2.4	5.3	3.5	0.41	-0.18	-0.17	0.38	0.11
Surface Temp. (K)	Global	4	3.7	3.6	3.9	3.8	0.033	-0.013	-0.021	-0.002	-0.001
	North Hemi.	4.9	4	3.7	4.6	4.3	0.035	-0.07	-0.044	-0.061	-0.035
	South Hemi.	3.1	3.3	3.5	3.3	3.3	0.031	0.044	0.002	0.057	0.033

Table 4-1: Seasonally-averaged responses to CO_2 concentration doubling. Top table is over land area, while bottom table is over all surface area in the domain. ΔControl indicates the 560 ppm CO_2 simulation minus the 280 ppm CO_2 simulation without code modifications, and likewise for ΔSnowVeg. The color highlights relative magnitude in each box.

%/K, 0.2 %/K, and 0.5 %/K respectively for the same seasons [*Qu and Hall*, 2014]. The CLM control values are well within the standard deviation reported. Annual mean surface albedo feedback was weaker with SnowCanVeg than without, by 4% globally and 5% in the North Hemisphere relative to ΔControl. There were no statistically significant differences in the mean climate sensitivity with a p-value of 0.05.

The climate response difference between the SnowVegCan simulation and unmodified simulation with CO_2 forcing is significantly smaller than the climate response differences between forcings, as seen in the net top-of-model (TOM) solar radiation (Figure 4-3). Mean global annual ΔEvolution was 0.00 K for surface temperature, and 0.0005 for total surface albedo (Table 4-1). Spatial and temporal shifts in ΔEvolution temperature, however, were significant (Figure 4-1, right). Extratropical NH land experienced a +0.34 K winter and -0.21 K spring change in ΔEvolution temperature response. Boreal winter shows the largest absolute magnitude temperature changes over land, with north boreal forests being most affected by the SnowVegCan modifications. An apparent high-latitude zonal dipole appears during this season (Figure 4-1, upper right). The North American continent between approximately 40-70°N experienced a negative ΔEvolution temperature change, while Eurasia experienced an increase in the same zonal range. Employing the regional domains analyzed in Chapter 3, the temperature difference is -1.4 K in East Boreal America, or -14% relative to ΔControl. Meanwhile, Western Siberia experienced a +2.3 K change in ΔEvolution, or +33% relative to ΔControl. However, there's no apparent correspondence to winter albedo differences (Figure 4-2, upper right). Neither net longwave nor total net radiation (not shown) exhibit a similar zonal dipole, suggesting that

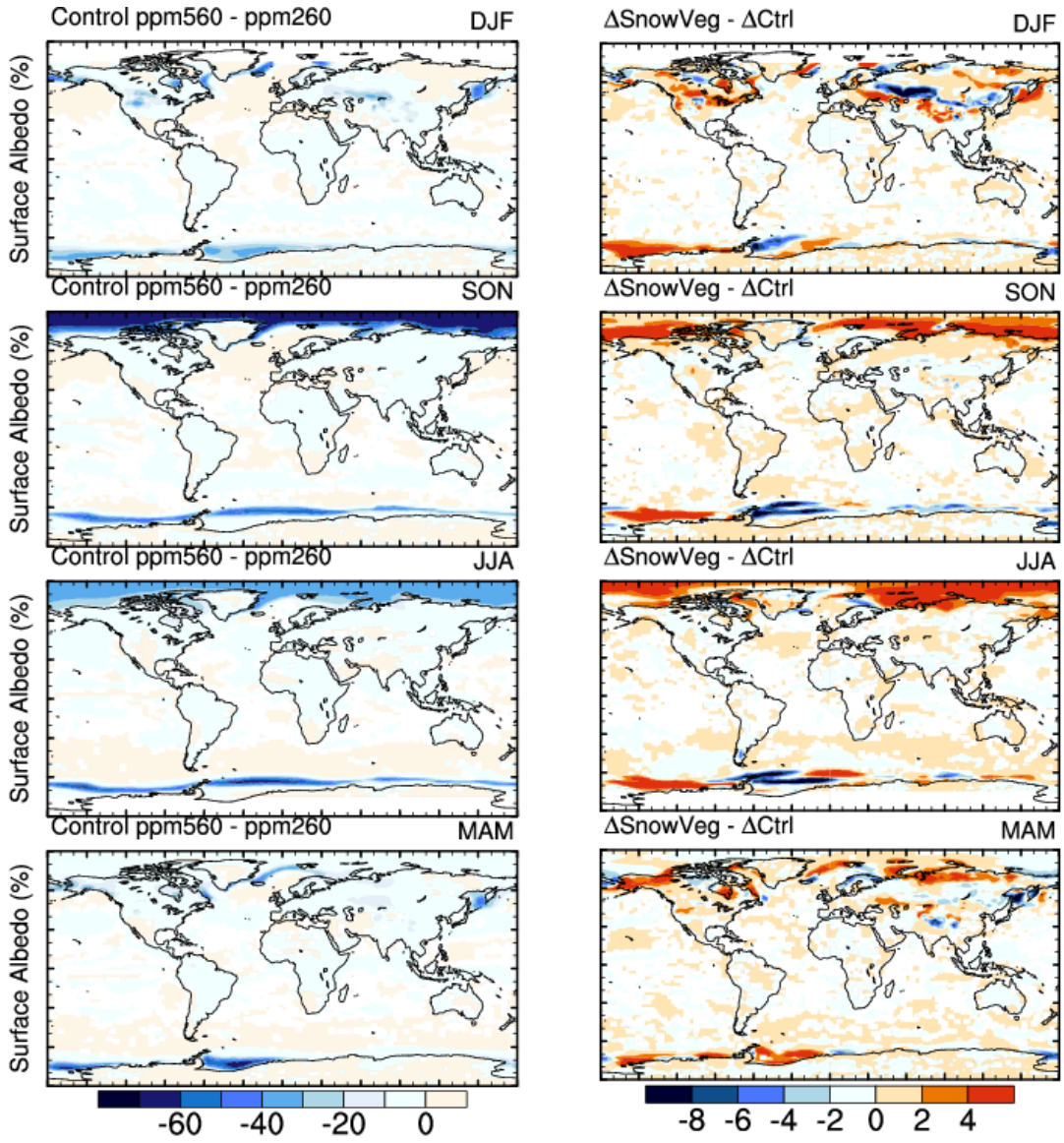

Figure 4-2: Similar to Figure 4-1, but for all-sky albedo.

the anomaly is not an albedo-radiation effect, but arising from a dynamic circulation influence.

		Land ΔEvolution/ΔControl (%)				
Variable	Domain	DJF	MAM	JJA	SON	ANN
Albedo	Global	1.3	-1.3	-1.9	-7.9	-0.052
	North Hemi.	1.3	-2.1	-4.9	-7.6	-0.64
	South Hemi.	0.13	31	40	-29	20
Downwelling Surf. SW	Global	6.5	44	-42	1.1	32
	North Hemi.	14	-5.5	-48	10	12
	South Hemi.	-6.7	-170	-34	31	-170
FSR	Global	1.2	2.7	6.8	3.5	2.9
	North Hemi.	2.5	-1.5	4.2	6	1.4
	South Hemi.	-1.7	330	-94	-7.2	12
SABV	Global	-100	-50	-5.6	25	-11
	North Hemi.	-13	9.7	2	-12	13
	South Hemi.	28	-84	-35	5.5	-25
Snow Frac.	Global	5.3	-1.2	-5	3.4	2.1
	North Hemi.	5.2	-1.4	-7.7	3.4	1.8
	South Hemi.	8.1	6.1	54	6.3	15
Snowcover Days	Global	4.4	-1.4	-4.3	0.9	-1
	North Hemi.	4.5	-1.7	-5.2	0.82	-1.3
	South Hemi.	3.5	4.4	21	4.8	5.3
Surface Temp.	Global	2.7	-1.8	-2.8	1	-0.082
	North Hemi.	4.1	-1.7	-1.5	0.88	0.67
	South Hemi.	-1.8	-1.9	-5.4	1.4	-1.9
Veg. Temp.	Global	2.6	-1.8	-3	0.8	-0.24
	North Hemi.	3.9	-1.6	-1.7	0.55	0.51
	South Hemi.	-1.6	-2.2	-5.6	1.4	-2

		ΔEvolution/ΔControl (%)				
Variable	Domain	DJF	MAM	JJA	SON	ANN
Albedo	Global	-1.9	-2.1	-5.9	-4.7	-3.7
	North Hemi.	-1.6	-1.5	-9.9	-14	-6.1
	South Hemi.	-2.5	-3.4	0.57	2.5	-0.14
Net TOM SW	Global	14	1.6	-5.5	1.4	1.6
	North Hemi.	19	5.7	-5	-9.2	0.51
	South Hemi.	10	-7.3	-7	7.2	3.1
Surface Temp.	Global	0.81	-0.36	-0.59	-0.062	-0.026
	North Hemi.	0.7	-1.8	-1.2	-1.3	-0.82
	South Hemi.	0.99	1.3	0.045	1.7	1

Table 4-2: Similar to Table 4-1. ΔEvolution, expressed as a percent change relative to ΔControl.

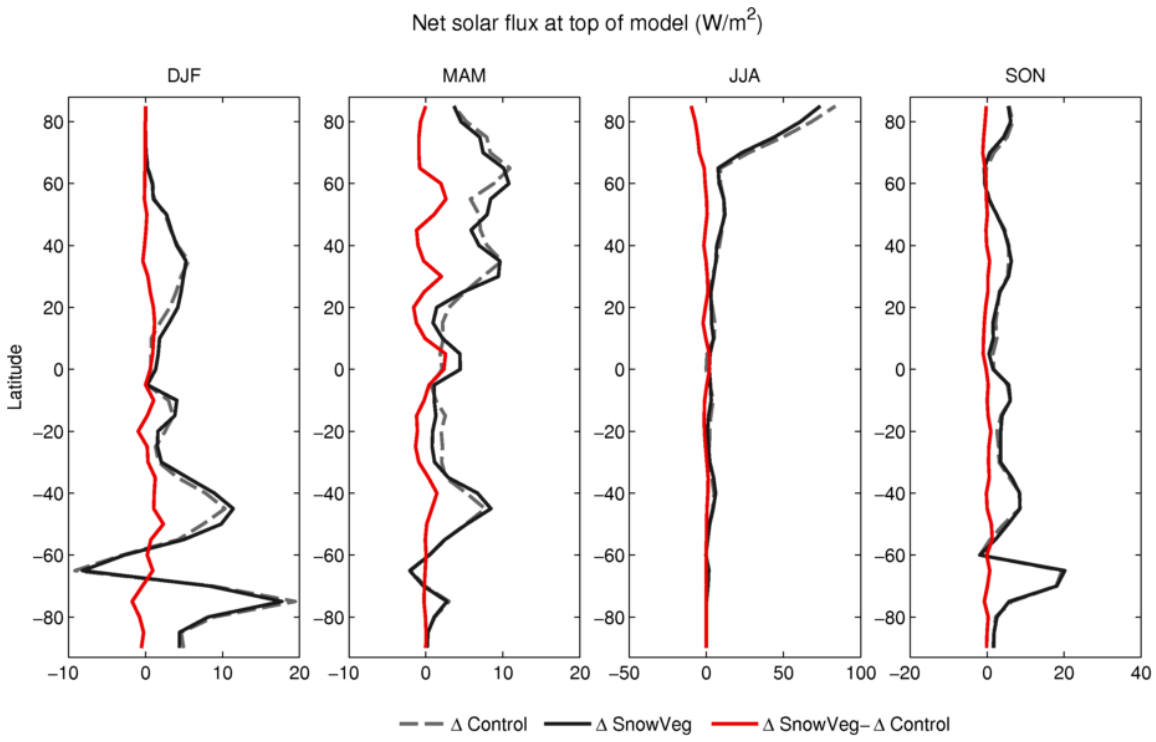

Figure 4-3: Equilibrium changes in net solar flux at top of model.

Sea ice extent alterations also result in strong regional and seasonal sensitivity. The autumn (SON) Arctic sea ice decreases most sharply. Meanwhile Antarctic sea ice sensitivity is not uniform in sign. There is a strong decrease in ΔEvolution temperature in the Ross Sea, and a strong increase south of the Weddell Sea during austral winter. The signal continues into austral spring.

We also calculate the duration of snow cover in each season (Figure 4-4). ΔControl duration decreases the most in autumn, by 1.4 days averaged over all North Hemisphere land, and by 2.6 days over the extratropical NH. Compared with ΔControl, ΔSnowveg duration is 0.12 days (10%) shorter in winter, and 0.07 days (5.2%) longer in summer in the extratropical NH (Table 4-1, Table 4-2). Temperature mid-latitude North American winter see increases in ΔEvolution snow duration, while the southern extent of the

Palearctic boreal forest experienced strong decreases (Figure 4-4). The winter Eurasian ΔEvolution snow cover duration correlates well with winter ΔEvolution albedo difference, both having a negative anomaly immediately north of a positive anomaly stretch across East-Central Russia. Vegetation masking effects are one possible explanation for such a winter signal. However, the coniferous arboreal-dominating region (Figure 4-5, bottom) does not extend south enough to cause the border between positive and negative anomalies. The ΔEvolution snowfall rate correlates fairly well with both snow cover duration and

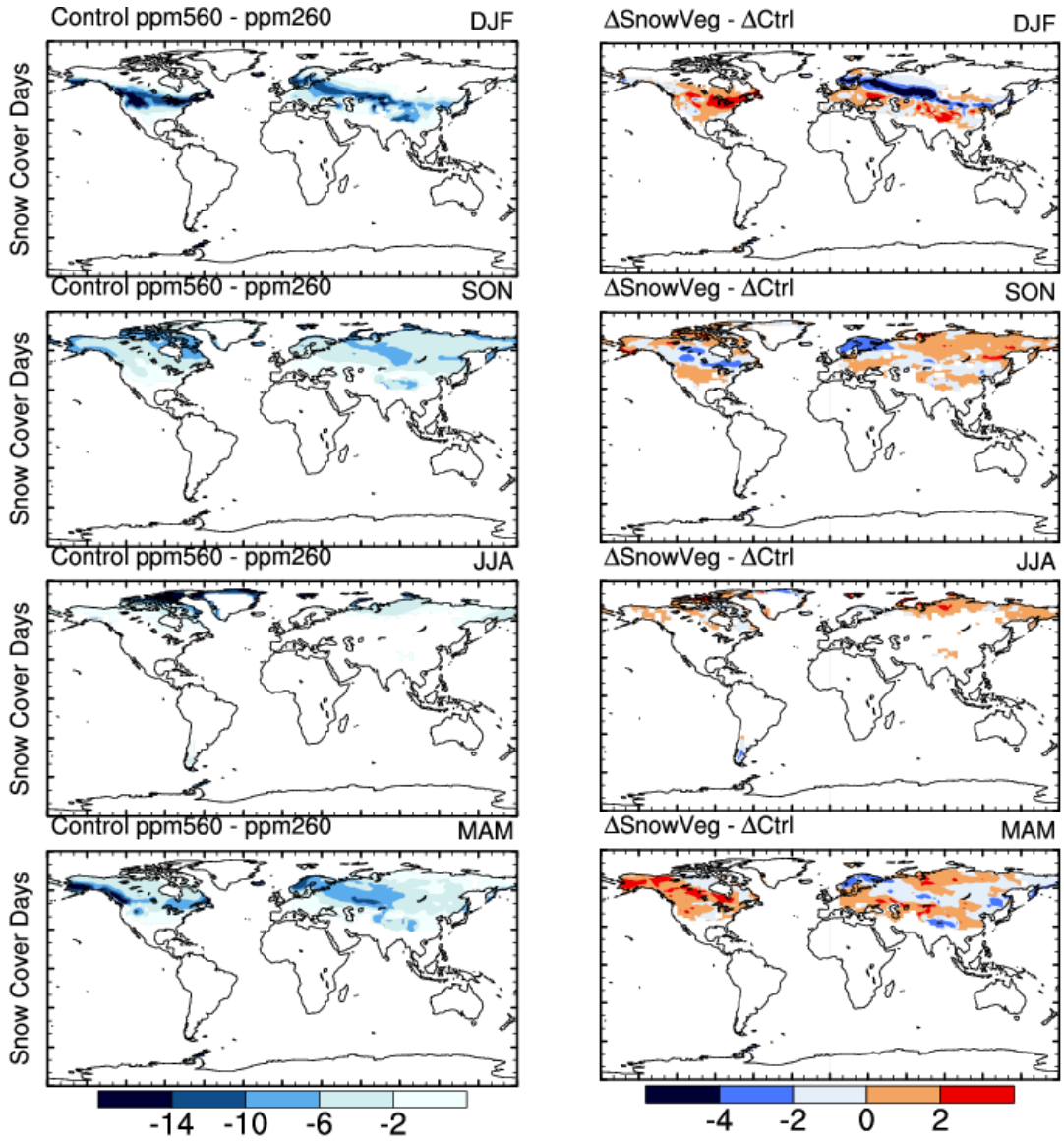

Figure 4-4: Similar to Figure 4-1, but for duration of snow cover, in days.

albedo in that region, indicating changing precipitation patterns in the coupled simulation are at least partially responsible.

4.4 Conclusions

The implementation of the snow vegetation code discussed in Chapter 3 resulted in no statistically significant change in the global climate sensitivity of the Community Earth System Model version 1.2, in response to a CO_2 concentration doubling from pre-industrial values. Global and boreal surface albedo feedback strength was slightly affected. The spatial variability of model response difference was considerable. Altered circulation patterns seemed to cause differences in regionally-specific albedo and snow cover duration differences between ΔSnowVeg and ΔControl. More rigorous investigation is required to explain if coupled model atmosphere and ocean dynamics are more responsible than shifts in the land radiation budget caused by vegetation masking changes.

The vegetation response to changing climate is an important feedback not considered in this study, Migration of boreal forests northward and the shrubification of the tundra would be an expected response to elevated CO_2 concentrations, thus strengthening the vegetation-snow masking effect. Comparison with Chapter 3 could not directly be made due to differences in land model versions. CESM in some configurations offers a dynamic vegetation model that is also not currently available in these types of coupled simulations. When CESM code infrastructure is able to support CLM4.5 in the "B" coupled model component sets, these analyses can be conducted.

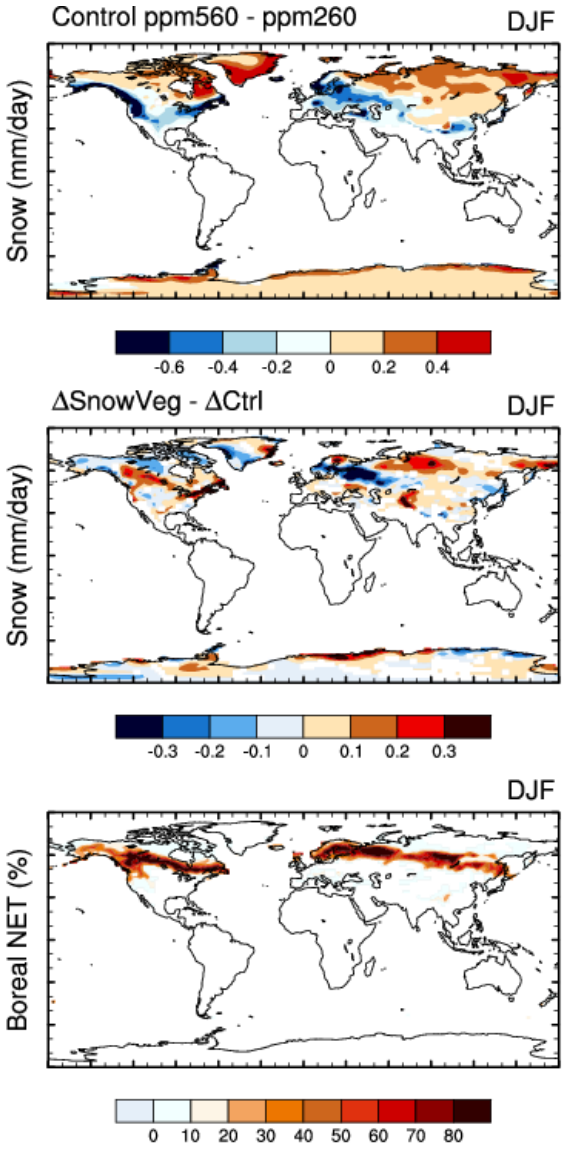

Figure 4-5: Top: ΔControl winter snowfall rate difference. Middle: ΔEvolution winter snowfall rate difference. Bottom: Percent land covered by the boreal needleleaf evergreen plant functional type.

Chapter 5

Conclusions and Future Work

5.1 Summary of Research

Accurate understanding and representation of cryosphere surfaces in GCMs are necessary to conduct realistic climate simulations, due to the strong feedback cycles associated with them. In addition to the classic snow and ice-albedo feedbacks, there are important biosphere-cryosphere interactions. As discussed, vegetation masking plays a large role in modulating the impact of the cryosphere on planetary albedo.

In Chapter 2, we discuss the design and implementation of a cryosphere radiative effect diagnostic in the CESM/CCSM models. This metric allowed us to quantify the instantaneous influence of sea ice, glaciers, and snow on the shortwave radiation budget, factoring the effects of cloud masking. In comparison with observationally-derived metrics, we found that the CESM/CCSM models represent these effects fairly accurately in the North Hemisphere. Over the 21st century, radiative forcing in the Representative Concentration Pathway (RCP) 8.5 scenario causes reduced boreal sea ice cover, austral sea ice cover, and boreal snow cover, which all contribute roughly equally to enhancing global absorbed shortwave radiation by 1.4–1.8 W m^{-2}. Twenty-first century RCP8.5 global cryospheric albedo feedbacks are +0.41 and +0.45 W m^{-2} K^{-1}, indicating that the two models exhibit similar temperature-normalized CrRE change.

Chapter 3 addresses the weak Community Land Model surface albedo feedback in boreal forest regions compared to satellite observations. We incorporated a modified canopy scheme into CLM4.5 with snow interception as a prognostic variable and snow unloading tuned to in-situ measurements. The canopy radiation scheme has been updated from a hard-wired temperature dependence, with optical parameters now directly related to the prognostic snow storage. With these model improvements implemented globally, boreal forest zones show a 27% reduction in winter visible direct shortwave RMSE relative to MODIS observations, and 13% reduction in spring RMSE. Spring improvements result from a more gradual seasonal transition in albedo attributed to the elimination of temperature-dependent canopy optical properties. Over the North Hemisphere land area, cumulative gridcell error was reduced 4% for net surface shortwave flux and 9% for visible direct albedo.

Chapter 4 continues the vegetation canopy snow (SnowVegCan) work of Chapter 3 by assessing the equilibrium climate sensitivity in CO_2 concentration doubling experiments. The Community Earth System Model version 1.2.0 (CESM1.2) was run in a pre-industrial configuration with CLM 4.0, with and without SnowVegCan implemented. There was little difference found between SnowVegCan-affected climate evolution and unmodified climate evolution, in terms of global annually-averaged temperature differences, surface albedo feedback strength, or climate sensitivity. Significant seasonally- and regionally-specific differences were observed, hinting at alterations in atmospheric and marine circulation caused by SnowVegCan.

5.2 Future Work

The CrRE metric is particularly well suited to partition different radiative components of cryospheric feedback in modeling scenarios. A future planned study will assess how land use change impacts snow radiative forcing. The impacts of shrinking snow cover in future scenarios of land use radiative forcing will be incorporated in the study.

The snow canopy vegetation implementation shows strong improvement in boreal forests, but further refinement can be made to improve biases globally. The incorporation of vegetation snowmelt-related energy fluxes can better represent under-canopy turbulent energy balance, an important influence on surface snow cover fraction not yet considered. Incorporation of observations from different vegetation sites and making interception parameters specific to plant functional type will more accurately predict snow albedo, especially in mid-latitude regions. CESM infrastructure does not currently support CLM4.5 in the "B" coupled model component sets. SnowVegCan is currently being implemented into the shared CLM4.5/5.0 codebase, and fully-coupled climate sensitivity experiments can easily be re-conducted once the framework is established. The assessment of SnowVegCan on land use and land cover change in coupled simulations is also a future consideration. With and without prescribed temporal land cover change, the CrRE diagnostic can be employed to assess the instantaneous shortwave radiative influence of vegetation-masked snow in coupled simulations.

Appendix A

Surface Radiative Kernels

A.1 Why are Radiative Kernels Useful?

A method to partition climate feedbacks with great utility for model intercomparisons was developed as described in *Soden and Held* [2006]. It splits feedbacks into a radiative kernel, which contains the assessment of top-of-atmosphere (TOA) change in fluxes due to a set perturbation from a desired feedback variable, and the response in climate to that feedback variable. Radiative kernels have been calculated for surface temperature, atmospheric temperature, water vapor, albedo, and CO_2 forcing.

The strength of this design is that it only needs to be calculated once, and can be used repeatedly to compare feedbacks in a model with different climate configurations. It also can be used to assess feedbacks between existing outputs from different climate models. Without this approach, each model in a comparison would have to generate new radiation calculations to be evaluated with each other, a potentially large computational expense. The partial radiative perturbation (PRP) is one method of doing this. It requires both an experimental run with forcing, as well as a control run.

A.2 What are Radiative Kernels?

As detailed in *Shell et al.* [2008], the feedback parameter associated with a TOA radiative forcing for a climate in equilibrium can be written as:

$$\gamma = \frac{\Delta(F-Q)}{\Delta T} \tag{28}$$

where $\Delta(F-Q)$ is the changes in longwave (terrestrial-sourced) and shortwave (solar-sourced) radiation necessary to keep the system in a steady state. This in turn can be viewed as a sum of factors affecting the TOA energy budget:

$$\gamma = \sum_{i=1}^{n} \frac{\partial(F-Q)}{\partial X_i} \frac{dX_i}{dT_s} + \text{small residual} \tag{29}$$

The factors represented in X are surface temperature, surface albedo, water vapor, and clouds. The differential $\frac{\partial(F-Q)}{\partial X_i}$ is the radiative kernel, containing the perturbation in X and the resulting change in shortwave and longwave fluxes. The derivative $\frac{dX_i}{dT_s}$ is the related feedback response.

A.3 Calculation of Surface Albedo Calculation

Computationally, the kernel $\frac{\partial(F-Q)}{\partial X_i}$ translates into perturbing albedo a small amount (selected to be +0.01 for comparability of CrRE work with a prior study) for every model gridcell, and then differencing the unaffected and affected flux. The reflectivities for four albedo bands were perturbed simultaneously: shortwave direct, shortwave diffuse, longwave direct, and longwave diffuse. Kernels were generated for two model configurations: CCSM4/CAM4 and CESM1/CAM5. Fully coupled model simulations

(with active land, atmosphere, ocean and river models with prognostic sea ice) were conducted for 2 years with an approximately one degree finite volume grid. For each model time-step, the radiative transfer scheme was conducted twice: once with the albedo perturbation, which does not affect the climate state, and again without the perturbation, which does. The computed radiative kernel is then found by dividing the difference in fluxes by the albedo perturbation. The methodology differs slightly from that of *Shell et al.* [2008] in that we generated instantaneous top-of-model (TOM) flux changes in a fully coupled model instead of an offline radiation calculation.

A.4 Employment and Study of CAM radiative kernels

We generated radiative kernels with clear-sky and all-sky conditions. Here we briefly describe their shortwave behavior. The simultaneous calculation of clear-sky (effect of clouds removed) and all-sky fluxes proved useful for the evaluation of the cryosphere (domain of snow and ice on the Earth's surface) shortwave radiation effects (Chapter 2). Surface and top-of-atmosphere shortwave fluxes appear in Figure A-1 and Figure A-2. The differences in fluxes also well as the radiative forcing of the albedo perturbation appear in Figure A-3.

First, very small (~0.1%) differences between the models appear in clear-sky downwelling flux at the surface (Figure A-1, right two columns; Figure A-3, upper right). These minor changes are due to differences in the assumptions between CAM4's delta-Eddington two-stream radiative transfer scheme and CAM5's modified correlated k-distribution band model, RRTMG. Not surprisingly, the radiative forcing strength,

associated with albedo perturbations, is proportional to the downwelling flux magnitude. Cloud influences caused a heterogeneous mix of positive and negative downwelling differences between models, with uniformly larger downwelling flux difference near the poles (Figure A-3, upper left). Differences in cloud treatment in these models are described in *Kay et al.* [2011] and *Kay et al.* [2012].

Differences in TOA fluxes show the largest change (by percent) occurs over Antarctica in both all-sky and clear-sky conditions (Figure A-2, bottom row). Compared to CAM4, clear-sky TOA net shortwave change in CAM5 is larger over marine ice-affected regions, as well as the Tibetan plateau Figure A-3, second column). Including the effects of clouds, CAM5 net radiative response is less over middle and lower latitude landmasses while higher over sea ice and over tropical and temperate marine areas (Figure A-3, first column). CAM5 increases clear-sky net shortwave response over low-latitude desert and tropical forest areas, while decreases over the Tibetan plateau (Figure A-3, 4th column). All-sky net shortwave response is decreased in CAM5 over marine ice-affected regions compared to CAM4, as well as downwelling flux response at the surface. Africa and South America show increases, while North America Eurasia are more mixed when comparing the two model versions. A stronger CAM5 signal for both net surface and net TOA shortwave response spreads across the oceans at approximately 50° S, and the influence of cloud changes in the intertropical convergence zone can be seen (Figure A-3, 3rd column).

The kernels have utility outside the author's research. Research by Adam Schneider (*In prep*) employs them to assess the multi-decadal temporal evolution of surface albedo feedback in over 30 CMIP5 models. The kernels enable comparisons in SAF variability in both historical and RCP 8.5 future warming scenarios. An investigation of 0.05 degree

MODIS data employed the kernels to provide CrRE estimates for 3 climate models [*Singh et al.*, 2015].

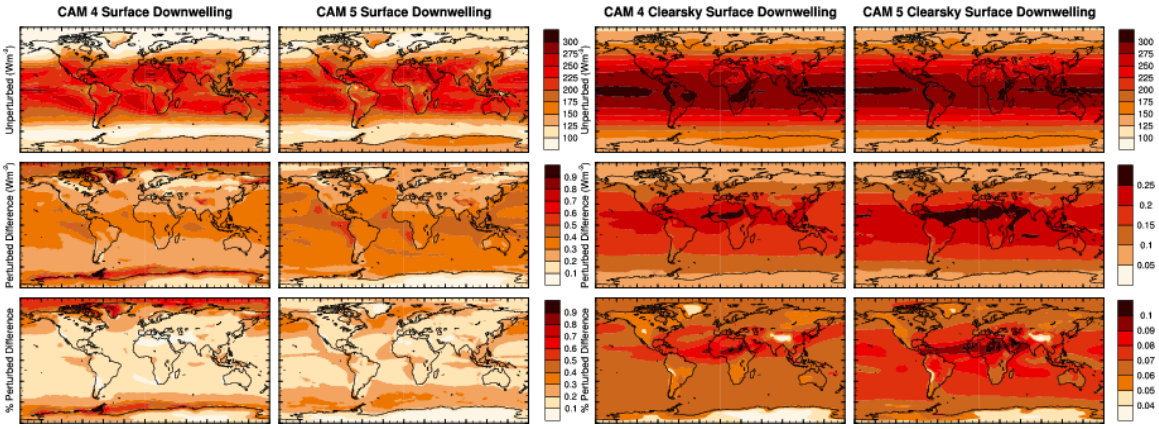

Figure A-1: Net Downwelling surface flux in all-sky conditions (left 2 columns) and clear-sky conditions (right 2 columns) for CAM4 and CAM5. Unperturbed fluxes appear in the top row, difference between unperturbed fluxes and perturbed fluxes appear in the middle row, and the percent difference appear in the bottom row.

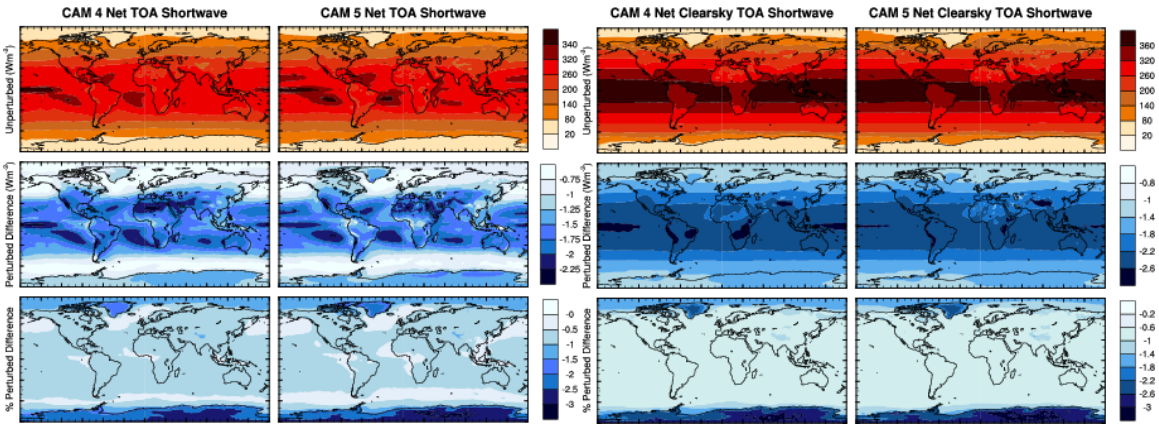

Figure A-2: Net Top-of-atmosphere (TOA) flux in all-sky conditions (left 2 columns) and clear-sky conditions (right 2 columns) for CAM4 and CAM5. Unperturbed fluxes appear in the top row, difference between unperturbed fluxes and perturbed fluxes appear in the middle row, and the percent difference appear in the bottom row.

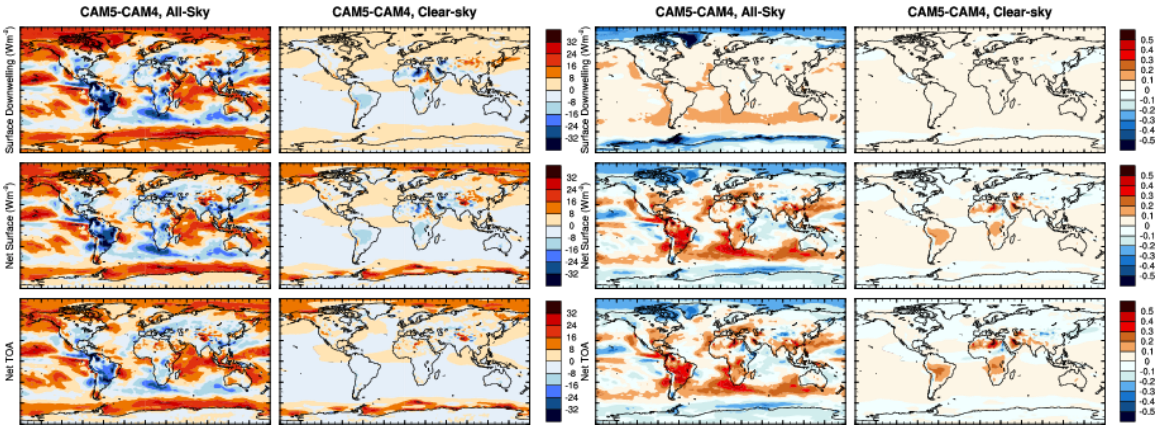

Figure A-3: Left two columns are difference in shortwave fluxes between CAM5 and CAM4 for both all-sky and clear-sky conditions. Right two columns are the intermodel differences in the radiative forcing of the perturbation. Top row contains surface downwelling flux, middle rowcontains net surface flux, and bottom row contains net top-of-atmosphere shortwave flux.

Bibliography

Andreadis, K. M., P. Storck, and D. P. Lettenmaier (2009), Modeling snow accumulation and ablation processes in forested environments, *Water Resour. Res.*, *45*(5), doi:10.1029/2008WR007042.

Arking, A. (1991), The radiative effects of clouds and their impact on climate, *Bull. Am. Meteorol. Soc.*, *71*(6), 795–813, doi:10.1175/1520-0477(1991)072<0795:TREOCA>2.0.CO;2.

Bergengren, J. C., S. L. Thompson, D. Pollard, and R. M. Deconto (2001), Modeling global climate-vegetation interactions in a doubled CO2 world, *Clim. Change*, *50*(1-2), 31–75, doi:10.1023/A:1010609620103.

Betts, A. K., J. H. Ball, and J. H. McCaughey (2001), Near-surface climate in the boreal forest, *J. Geophys. Res.*, *106*(D24), 33529, doi:10.1029/2001JD900047.

Bitz, C. M., and S. J. Marshall (2012), Cryosphere, Modeling of, in *Climate Change Modeling Methodology*, 1, pp. 31–62, Springer.

Bøggild, C. E., R. E. Brandt, K. J. Brown, and S. G. Warren (2010), The ablation zone in northeast Greenland: ice types, albedos and impurities, *J. Glaciol.*, *56*, 101–113, doi:10.3189/002214310791190776.

Bonan, G. B., D. Pollard, and S. L. Thompson (1992), Effects of boreal forest vegetation on global climate, *Nature*, *359*(6397), 716–718, doi:10.1038/359716a0.

Bonfils, C. J. W., T. J. Phillips, D. M. Lawrence, P. Cameron-Smith, W. J. Riley, and Z. M. Subin (2012), On the influence of shrub height and expansion on northern high latitude climate, *Environ. Res. Lett.*, *7*(1), 015503, doi:10.1088/1748-9326/7/1/015503.

Bony, S. et al. (2006), How Well Do We Understand and Evaluate Climate Change Feedback Processes?, *J. Clim.*, *19*(15), 3445–3482, doi:10.1175/JCLI3819.1.

Boone, A., and P. Etchevers (2001), An Intercomparison of Three Snow Schemes of Varying Complexity Coupled to the Same Land Surface Model: Local-Scale Evaluation at an Alpine Site, *J. Hydrometeorol.*, *2*(4), 374–394, doi:10.1175/1525-7541(2001)002<0374:AIOTSS>2.0.CO;2.

Box, J. E., X. Fettweis, J. C. Stroeve, M. Tedesco, D. K. Hall, and K. Steffen (2012), Greenland ice sheet albedo feedback: thermodynamics and atmospheric drivers, *Cryosph.*, *6*(4), 821–839, doi:10.5194/tc-6-821-2012.

Briegleb, B., and B. Light (2007), A Delta-Eddington multiple scattering parameterization for solar radiation in the sea ice component of the Community Climate System Model, *NCAR Tech. Note NCAR/TN-472+STR*, doi:10.5065/D6B27S71.

Bryan, K. (1969), Climate and the Ocean Circulation III. The Ocean Model, *Mon. Weather Rev.*, *97*(11), 806–827, doi:10.1175/1520-0493(1969)097<0806:CATOC>2.3.CO;2.

Budyko, M. I. (1969), The effect of solar radiation variations on the climate of the Earth, *Tellus*, *21*(5), 611–619, doi:10.1111/j.2153-3490.1969.tb00466.x.

Chalita, S., and H. Le Treut (1994), The albedo of temperate and boreal forest and the Northern Hemisphere climate: a sensitivity experiment using the LMD GCM, *Clim. Dyn.*, *10*(4-5), 231–240, doi:10.1007/BF00208990.

Chen, F. et al. (2014), Modeling seasonal snowpack evolution in the complex terrain and forested Colorado Headwaters region: A model intercomparison study, *J. Geophys. Res. Atmos.*, *119*, doi:10.1002/2014JD022167.

Clark, M. P. et al. (2015a), A unified approach for process-based hydrologic modeling: 1. Modeling concept, *Water Resour. Res.*, *51*(4), doi:10.1002/2015WR017198.

Clark, M. P. et al. (2015b), A unified approach for process-based hydrologic modeling: 2. Model implementation and case studies, *Water Resour. Res.*, *51*(4), doi:10.1002/2015WR017200.

Deardorff, J. W. (1978), Efficient prediction of ground surface temperature and moisture, with inclusion of a layer of vegetation, *J. Geophys. Res.*, *83*(C4), 1889, doi:10.1029/JC083iC04p01889.

Donohoe, A., and D. S. Battisti (2011), Atmospheric and Surface Contributions to Planetary Albedo, *J. Clim.*, *24*(16), 4402–4418, doi:10.1175/2011JCLI3946.1.

Douville, H., and J.-F. Royer (1996), Influence of the temperate and boreal forests on the Northern Hemisphere climate in the Météo-France climate model, *Clim. Dyn.*, *13*(1), 57–74, doi:10.1007/s003820050153.

Essery, R. (2013), Large-scale simulations of snow albedo masking by forests, *Geophys. Res. Lett.*, *40*, 5521–5525, doi:10.1002/grl.51008.

Essery, R., E. Martin, H. Douville, A. Fernandez, and E. Brun (1999), A comparison of four snow models using observations from an alpine site, *Clim. Dyn.*, *15*(8), 583–593.

Essery, R., N. Rutter, J. Pomeroy, R. Baxter, M. Stähli, D. Gustafsson, A. Barr, P. Bartlett, and K. Elder (2009), SNOWMIP2: An Evaluation of Forest Snow Process Simulations, *Bull. Am. Meteorol. Soc.*, *90*(8), 1120–1135, doi:10.1175/2009BAMS2629.1.

Etheridge, D. M., L. P. Steele, R. L. Langenfelds, R. J. Francey, J.-M. Barnola, and V. I. Morgan (1996), Natural and anthropogenic changes in atmospheric CO 2 over the last 1000 years from air in Antarctic ice and firn, *J. Geophys. Res.*, *101*(D2), 4115, doi:10.1029/95JD03410.

Feng, X., A. Sahoo, and K. Arsenault (2008), The impact of snow model complexity at three CLPX sites, *J. Hydrometeorol.*, *9*(6), 1464–1481.

Fierz, C. et al. (2003), SNOWMIP, an intercomparison of snow models : comparison of simulated and observed internal state International, in *Workshop on Snow Processes: Representation in Atmospheric and Hydrological Models (International Commission on Snow & Ice IAHS/IAMAS), XXIII General Assembly of the International Union of Geodesy and Geophysics IUGG*.

Flanner, M. G., and C. S. Zender (2006), Linking snowpack microphysics and albedo evolution, *J. Geophys. Res. Atmos.*, *111*(12), doi:10.1029/2005JD006834.

Flanner, M. G., C. S. Zender, J. T. Randerson, and P. J. Rasch (2007), Present-day climate forcing and response from black carbon in snow, *J. Geophys. Res.*, *112*(D11), D11202, doi:10.1029/2006JD008003.

Flanner, M. G., K. M. Shell, M. Barlage, D. K. Perovich, and M. A. Tschudi (2011), Radiative forcing and albedo feedback from the Northern Hemisphere cryosphere between 1979 and 2008, *Nat. Geosci.*, *4*(3), 151–155, doi:10.1038/ngeo1062.

Fletcher, C. G., H. Zhao, P. J. Kushner, and R. Fernandes (2012), Using models and satellite observations to evaluate the strength of snow albedo feedback, *J. Geophys. Res.*, *117*(D11), D11117, doi:10.1029/2012JD017724.

Fletcher, C. G., C. W. Thackeray, and T. M. Burgers (2015), Evaluating biases in simulated snow albedo feedback in two generations of climate models, *J. Geophys. Res. Atmos.*, *120*(1), 12–26, doi:10.1002/2014JD022546.

Gallimore, R. G., and J. E. Kutzbach (1996), Role of orbitally induced changes in tundra area in the onset of glaciation, *Nature*, *381*(6582), 503–505, doi:10.1038/381503a0.

Gent, P. R. et al. (2011), The Community Climate System Model Version 4, *J. Clim.*, *24*(19), 4973–4991, doi:10.1175/2011JCLI4083.1.

Glen, J. W. (1955), The Creep of Polycrystalline Ice, *Proc. R. Soc. A Math. Phys. Eng. Sci.*, *228*(1175), 519–538, doi:10.1098/rspa.1955.0066.

Hays, J. D., J. Imbrie, and N. J. Shackleton (1976), Variations in the Earth's Orbit: Pacemaker of the Ice Ages., *Science*, *194*(4270), 1121–32, doi:10.1126/science.194.4270.1121.

Henderson-Sellers, A., and M. F. Wilson (1983), Surface albedo data for climatic modeling, *Rev. Geophys. 21*(8), 1743, doi:10.1029/RG021i008p01743.

Holland, M. M., D. A. Bailey, B. P. Briegleb, B. Light, and E. Hunke (2012), Improved Sea Ice Shortwave Radiation Physics in CCSM4: The Impact of Melt Ponds and Aerosols on Arctic Sea Ice, *J. Clim.*, *25*(5), 1413–1430, doi:10.1175/JCLI-D-11-00078.1.

Hurrell, J. W. et al. (2013), The Community Earth System Model: A Framework for Collaborative Research, *Bull. Am. Meteorol. Soc.*, *94*(9), 1339–1360, doi:10.1175/BAMS-D-12-00121.1.

Jin, J., X. Gao, Z.-L. Yang, R. C. Bales, S. Sorooshian, R. E. Dickinson, S. F. Sun, and G. X. Wu (1999), Comparative Analyses of Physically Based Snowmelt Models for Climate Simulations, *J. Clim.*, *12*(8), 2643–2657, doi:10.1175/1520-0442(1999)012<2643:CAOPBS>2.0.CO;2.

Jordan, R. (1991), A one-dimensional temperature model for a snow cover: Technical documentation for SNTHERM.89, *CRREL Spec. Rep.*, *91-16*, 58.

Joseph, J. H., W. J. Wiscombe, and J. A. Weinman (1976), The Delta-Eddington Approximation for Radiative Flux Transfer, *J. Atmos. Sci.*, *33*(12), 2452–2459, doi:10.1175/1520-0469(1976)033<2452:TDEAFR>2.0.CO;2.

Kay, J. E., K. Raeder, A. Gettelman, and J. Anderson (2011), The Boundary Layer Response to Recent Arctic Sea Ice Loss and Implications for High-Latitude Climate Feedbacks, *J. Clim.*, *24*(2), 428–447, doi:10.1175/2010JCLI3651.1.

Kay, J. E., M. M. Holland, C. M. Bitz, E. Blanchard-Wrigglesworth, A. Gettelman, A. Conley, and D. Bailey (2012), The Influence of Local Feedbacks and Northward Heat Transport on the Equilibrium Arctic Climate Response to Increased Greenhouse Gas Forcing, *J. Clim.*, *25*(16), 5433–5450, doi:10.1175/JCLI-D-11-00622.1.

Lawrence, D. M., P. E. Thornton, K. W. Oleson, and G. B. Bonan (2007), The Partitioning of Evapotranspiration into Transpiration, Soil Evaporation, and Canopy Evaporation in a GCM: Impacts on Land–Atmosphere Interaction, *J. Hydrometeorol.*, *8*(4), 862–880, doi:10.1175/JHM596.1.

Lawrence, D. M. et al. (2011), Parameterization improvements and functional and structural advances in Version 4 of the Community Land Model, *J. Adv. Model. Earth Syst.*, *3*(3), 1–27, doi:10.1029/2011MS000045.

Lawrence, P. J., and T. N. Chase (2007), Representing a new MODIS consistent land surface in the Community Land Model (CLM 3.0), *J. Geophys. Res.*, *112*(G1), doi:10.1029/2006JG000168.

Loranty, M. M., L. T. Berner, S. J. Goetz, Y. Jin, and J. T. Randerson (2014), Vegetation controls on northern high latitude snow-albedo feedback: observations and CMIP5 model simulations., *Glob. Chang. Biol.*, *20*(2), 594–606, doi:10.1111/gcb.12391.

Mahat, V., and D. G. Tarboton (2013), Representation of canopy snow interception, unloading and melt in a parsimonious snowmelt model, *Hydrol. Process.*, *28*, 6320–6336, doi:10.1002/hyp.10116.

Manabe, S. (1969), Climate and the Ocean Circulation I. The Atmospheric Circulation and the Hydrology of the Earth's Surface, *Mon. Weather Rev.*, *97*(11), 739–774, doi:10.1175/1520-0493(1969)097<0739:CATOC>2.3.CO;2.

Mearns, L. O., M. S. Bukovsky, S. C. Pryor, and V. Magaña (2014), Downscaling of Climate Information, in *Climate Change in North America*, 1, pp. 201–250, Springer International Publishing, Cham.

Meehl, G. A., W. M. Washington, J. M. Arblaster, A. Hu, H. Teng, J. E. Kay, A. Gettelman, D. M. Lawrence, B. M. Sanderson, and W. G. Strand (2013), Climate Change Projections in CESM1(CAM5) Compared to CCSM4, *J. Clim.*, *26*(17), 6287–6308, doi:10.1175/JCLI-D-12-00572.1.

Meinshausen, M. et al. (2011), The RCP greenhouse gas concentrations and their extensions from 1765 to 2300, *Clim. Change*, *109*(1-2), 213–241, doi:10.1007/s10584-011-0156-z.

Myhre, G. et al. (2013), Anthropogenic and Natural Radiative Forcing, in *Climate Change 2013: The Physical Science Basis. Contribution of Working Group I to the Fifth Assessment Report of the Intergovernmental Panel on Climate Change*, 10, pp. 659–740, Cambridge University Press.

Niu, G.-Y., and Z.-L. Yang (2004), Effects of vegetation canopy processes on snow surface energy and mass balances, *J. Geophys. Res. Atmos.*, *109*(D23), n/a–n/a, doi:10.1029/2004JD004884.

Niu, G.-Y., and X. Zeng (2012), Earth System Model, Modeling the Land Component of, in *Climate Change Modeling Methodology*, 1, pp. 139–168, Springer.

Nye, J. F. (1963), The Response of a Glacier to Changes in the Rate of Nourishment and Wastage, *Proc. R. Soc. A Math. Phys. Eng. Sci.*, *275*(1360), 87–112, doi:10.1098/rspa.1963.0157.

Oleson, K. W. et al. (2013), *Technical Description of version 4.5 of the Community Land Model (CLM)*, Boulder, CO.

Perket, J., M. G. Flanner, and J. E. Kay (2014), Diagnosing shortwave cryosphere radiative effect and its 21st century evolution in CESM, *J. Geophys. Res. Atmos.*, *119*(3), 1356–1362, doi:10.1002/2013JD021139.

Pomeroy, J. W., D. M. Gray, K. R. Shook, B. Toth, R. L. H. Essery, A. Pietroniro, and N. Hedstrom (1998), An evaluation of snow accumulation and ablation processes for land surface modelling, *Hydrol. Process.*, *12*(15), 2339–2367.

Qian, T., A. Dai, K. E. Trenberth, and K. W. Oleson (2006), Simulation of global land surface conditions from 1948 to 2004. Part I: Forcing data and evaluations, *J. Hydrometeorol.*, *7*(5), 953–975.

Qu, X., and A. Hall (2007), What Controls the Strength of Snow-Albedo Feedback?, *J. Clim.*, *20*(15), 3971–3981, doi:10.1175/JCLI4186.1.

Qu, X., and A. Hall (2014), On the persistent spread in snow-albedo feedback, *Clim. Dyn.*, *42*(1-2), 69–81, doi:10.1007/s00382-013-1774-0.

Ramanathan, V., R. D. Cess, E. F. Harrison, P. Minnis, B. R. Barkstrom, E. Ahmad, and D. Hartmann (1989), Cloud-radiative forcing and climate: results from the Earth radiation budget experiment., *Science*, *243*(4887), 57–63, doi:10.1126/science.243.4887.57.

Renssen, H. (2003), On the non-linear response of the ocean thermohaline circulation to global deforestation, *Geophys. Res. Lett.*, *30*(2), 1061, doi:10.1029/2002GL016155.

Roe, G. H., and M. B. Baker (2007), Why is climate sensitivity so unpredictable?, *Science*, *318*(5850), 629–32, doi:10.1126/science.1144735.

Roesch, A., M. Wild, H. Gilgen, and A. Ohmura (2001), A new snow cover fraction parametrization for the ECHAM4 GCM, *Clim. Dyn.*, *17*(12), 933–946, doi:10.1007/s003820100153.

Schaaf, C. B. et al. (2002), First operational BRDF, albedo nadir reflectance products from MODIS, *Remote Sens. Environ.*, *83*(1-2), 135–148, doi:10.1016/S0034-4257(02)00091-3.

Schlosser, C. A., A. G. Slater, A. Robock, A. J. Pitman, K. Y. Vinnikov, A. Henderson-Sellers, N. A. Speranskaya, and K. Mitchell (2000), Simulations of a boreal grassland hydrology at Valdai, Russia: PILPS Phase 2 (d), *Mon. Weather Rev.*, *128*(2), 301–321.

Sellers, W. D. (1969), A Global Climatic Model Based on the Energy Balance of the Earth-Atmosphere System., *J. Appl. Meteorol.*, *8*(3), doi:10.1175/1520-0450(1969)008<0392:AGCMBO>2.0.CO;2.

Shell, K. M., J. T. Kiehl, and C. A. Shields (2008), Using the Radiative Kernel Technique to Calculate Climate Feedbacks in NCAR's Community Atmospheric Model, *J. Clim.*, *21*(10), 2269–2282, doi:10.1175/2007JCLI2044.1.

Singh, D., M. G. Flanner, and J. Perket (2015), The Global Land Cryosphere Radiative Effect during the MODIS era, *Cryosph.*, *submitted*.

Slater, A. G. et al. (2001), The Representation of Snow in Land Surface Schemes: Results from PILPS 2(d), *J. Hydrometeorol.*, *2*(1), 7–25, doi:10.1175/1525-7541(2001)002<0007:TROSIL>2.0.CO;2.

Soden, B. J., and I. M. Held (2006), An Assessment of Climate Feedbacks in Coupled Ocean–Atmosphere Models, *J. Clim.*, *19*(14), 3354–3360, doi:10.1175/JCLI3799.1.

Soden, B. J., I. M. Held, R. Colman, K. M. Shell, J. T. Kiehl, and C. A. Shields (2008), Quantifying Climate Feedbacks Using Radiative Kernels, *J. Clim.*, *21*(14), 3504–3520, doi:10.1175/2007JCLI2110.1.

Stephens, G. (2005), Cloud feedbacks in the climate system: A critical review, *J. Clim.*, *18*, 237–273.

Storck, P., D. P. Lettenmaier, and S. M. Bolton (2002), Measurement of snow interception and canopy effects on snow accumulation and melt in a mountainous maritime climate, Oregon, United States, *Water Resour. Res.*, *38*(11), 1223, doi:10.1029/2002WR001281.

Stroeve, J., J. E. Box, Z. Wang, C. Schaaf, and A. Barrett (2013), Re-evaluation of MODIS MCD43 Greenland albedo accuracy and trends, *Remote Sens. Environ.*, *138*, 199–214, doi:10.1016/j.rse.2013.07.023.

Thackeray, C. W., C. G. Fletcher, and C. Derksen (2014), The influence of canopy snow parameterizations on snow albedo feedback in boreal forest regions, *J. Geophys. Res. Atmos.*, *119*(16), 1–37, doi:10.1002/2014JD021858.

Thomas, G., and P. R. Rowntree (1992), The Boreal Forests and Climate, *Q. J. R. Meteorol. Soc.*, *118*(505), 469–497, doi:10.1002/qj.49711850505.

Vaughan, D. G. et al. (2013), Observations: Cryosphere, in *Climate Change 2013: The Physical Science Basis. Contribution of Working Group I to the Fifth Assessment Report of the Intergovernmental Panel on Climate Change*, 10, pp. 317–282, Cambridge University Press.

Winton, M. (2006), Amplified Arctic climate change: What does surface albedo feedback have to do with it?, *Geophys. Res. Lett.*, *33*(3), L03701, doi:10.1029/2005GL025244.

Wiscombe, W. J., and S. G. Warren (1980), A Model for the Spectral Albedo of Snow. I: Pure Snow, *J. Atmos. Sci.*, *37*(12), 2712–2733, doi:10.1175/1520-0469(1980)037<2712:AMFTSA>2.0.CO;2.